J. Fluid Mech. (1998), *vol.* 367, *pp.* 291–328. Printed in the United Kingdom

Joint probability density analysis of the structure and dynamics of the vorticity field of a turbulent boundary layer

By LAWRENCE ONG AND JAMES M. WALLACE

Department of Mechanical Engineering, University of Maryland, College Park, MD 20742, USA

(Received 18 April 1996 and in revised form 23 December 1997)

An experimental study of a turbulent boundary layer at $R_\theta \approx 1070$ and $R_\tau \approx 543$ was conducted. Detailed measurements of the velocity vector and the velocity gradient tensor within the near-wall region were performed at various distances from the wall, ranging from approximately $y^+ = 14$ to $y^+ = 89$. The measured mean statistical properties of the fluctuating velocity and vorticity components agree well with previous experimental and numerically simulated data. These boundary layer measurements were used in a joint probability density analysis of the various component vorticity and vorticity–velocity gradient products that appear in the instantaneous vorticity and enstrophy transport equations. The vorticity filaments that contribute most to the vorticity covariance $\overline{\Omega_x\Omega_y}$ in this region were found to be oriented downstream with angles of inclination to the wall, when projected on the streamwise (x, y)-plane, that decrease with distance moving from the buffer to the logarithmic layer. When projected on the planview (x, z)- and cross-stream (y, z)-planes, the vorticity filaments that most contribute to the vorticity covariances $\overline{\Omega_x\Omega_z}$ and $\overline{\Omega_y\Omega_z}$ have angles of inclination to the z-ordinate axis that increase with distance from it. All the elements of the $\Omega_i\Omega_j\partial U_i/\partial x_j$ term in the enstrophy transport equation, i.e. the term that describes the rate of increase or decrease of the enstrophy by vorticity filament stretching or compression by the strain-rate field, have been examined. On balance, the average stretching of the vorticity filaments is greater than compression at all y^+ locations examined here. However, some individual velocity gradient components compress the vorticity filaments, on average, more than they stretch them.

1. Introduction

Although a vast amount of information about the properties of the turbulent boundary layer and insight into its structure has been obtained during many decades of research, it only has been within the last decade that accurate knowledge of the vorticity field of this technically important flow has been obtained. This advance in our knowledge is a result of the development of adequate means to measure one or more components of the vorticity vector in turbulent flows (see Foss & Wallace 1989 and Wallace & Foss 1995) as well as the development of direct numerical simulations (DNS) of turbulent flows, both with sufficient resolution to account for most of the turbulent scales. The data bases resulting from these developments have made possible the examination of the terms in the transport equations for instantaneous

vorticity

$$\underbrace{\frac{\partial \Omega_i}{\partial t}}_{\text{I}} + \underbrace{U_j \frac{\partial \Omega_i}{\partial x_j}}_{\text{II}} = \underbrace{\Omega_j \frac{\partial U_i}{\partial x_j}}_{\text{III}} + \underbrace{\nu \frac{\partial^2 \Omega_i}{\partial x_j \partial x_j}}_{\text{IV}} \tag{1.1}$$

and enstrophy ($\frac{1}{2}\Omega_i\Omega_i$, a scalar measure of the vorticity magnitude)

$$\underbrace{\frac{\partial(\frac{1}{2}\Omega_i\Omega_i)}{\partial t}}_{\text{I}} + \underbrace{U_j \frac{\partial(\frac{1}{2}\Omega_i\Omega_i)}{\partial x_j}}_{\text{II}} = \underbrace{\Omega_i\Omega_j \frac{\partial U_i}{\partial x_j}}_{\text{III}} + \underbrace{\nu \frac{\partial^2(\frac{1}{2}\Omega_i\Omega_i)}{\partial x_j \partial x_j}}_{\text{IV}} - \underbrace{\nu \frac{\partial \Omega_i}{\partial x_j}\frac{\partial \Omega_i}{\partial x_j}}_{\text{V}}, \tag{1.2}$$

where the terms represent the (I) rate of change in the Ω_i component of vorticity or of enstrophy at an Eulerian location in the flow due to: (II) advection, (III) stretching/compression by reorientation, (IV) viscous diffusion and (V) viscous dissipation (summation over repeating indices is implied here and elsewhere).

Tennekes & Lumley (1989) have derived and interpreted the terms of transport equations for mean, $\frac{1}{2}\overline{\Omega_i\Omega_i}$, and turbulent, $\frac{1}{2}\overline{\omega_i\omega_i}$, enstrophy which are vorticity field analogues of the velocity field transport equations for mean and turbulent kinetic energy. Balint, Wallace & Vukoslavčević (1990, 1991) have shown how the terms in the mean and turbulent enstrophy equations relate to the terms in the equation for total enstrophy, which is the average of equation (1.2). They also measured the terms in all three of these equations and showed that viscous diffusion and dissipation of total enstrophy are the dominant processes in the buffer layer and lower part of the logarithmic layer, but that enstrophy production by stretching almost balances dissipation farther out in the logarithmic layer. Values of most of the measured terms of the turbulent enstrophy equation from the experiment of Balint *et al.* (1990) have been recently compared by Gorski, Wallace & Bernard (1994) to values obtained from a DNS of turbulent channel flow at $R_\tau(\equiv u_\tau h/\nu) = 145$ of Handler, Hendricks & Leighton. (1989). Here h is the channel half-width, the friction velocity $u_\tau \equiv [\tau_w/\rho]^{1/2}$, ρ is the fluid density, the shear stress at the wall $\tau_w \equiv \mu\partial\overline{U}/\partial y_{wall}$, and μ and ν are the fluid molecular and kinematic viscosities, respectively. Good agreement was found, leading Gorski *et al.* (1994) to conclude that these properties have common values for different types of bounded flows over at least a modest range of Reynolds numbers. They discussed the implications of this for two-equation modelling where the enstrophy transport equation can serve as a surrogate for the dissipation rate transport equation. Walker, Leighton & Garza-Rios (1996) have determined the turbulent enstrophy budget for a DNS of an open channel flow near its free surface, and Balint, Wallace & Vukoslavčević (1989) have measured the turbulent enstrophy budget terms for a two-stream mixing layer.

However, it seems that the physics of the transport processes represented mathematically by the vector and scalar terms in the transport equations (1.1) and (1.2) for instantaneous vorticity and enstrophy have not been systematically examined. Of particular interest are terms (III) in these two equations, because they represent, respectively, the rate of change in the vorticity components due to stretching/compression arising from reorientation of the vorticity filaments by the strain-rate field, and the concomitant rate of change of the contribution to the local enstrophy from each vorticity component. This paper aims to unravel the transport physics represented by terms (III). This will be accomplished by examining the joint probability density functions (JPDFs), $P(\Omega_j, \partial U_i/\partial x_j)$ and $P(\Omega_i, \Omega_j\partial U_i/\partial x_j)$. In addition, some insight

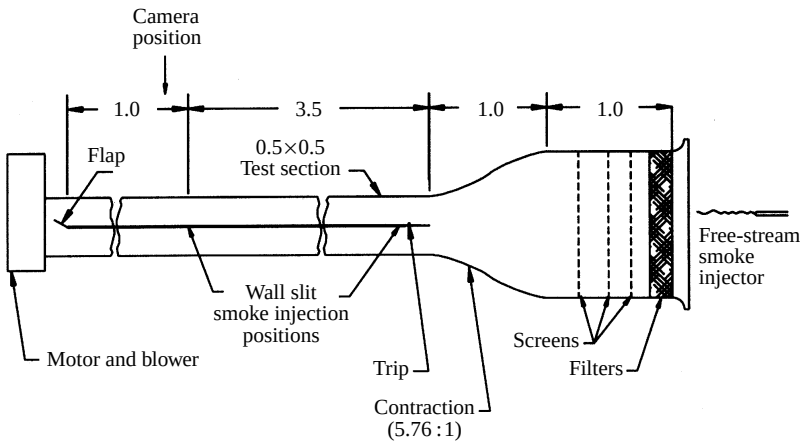

FIGURE 1. Wind tunnel at Ecole Centrale de Lyon. Dimensions in m.

into the structure of the vorticity field of the turbulent boundary layer and how it gives rise to the vorticity component covariances will be obtained by determining the JPDFs of the vorticity components, $P(\Omega_i, \Omega_j)$.

The experimental facility and instrumentation are described briefly in § 2, including the multi-sensor hot-wire probe used to simultaneously measure the velocity and vorticity vectors. In § 3 the distributions of some statistical properties of the velocity and vorticity components of this boundary layer are compared to values from earlier experiments and to values obtained from DNS in order to assess the quality of the present data. The JPDF analysis and interpretation is presented in § 4, and conclusions are drawn in § 5.

2. Experimental facility and instrumentation

The experiment was performed in the low-speed boundary layer wind tunnel, shown in the sketch in figure 1, at the Laboratoire de Mécanique des Fluides, Ecole Centrale de Lyon, France. A flat plate with a sharp leading edge is mounted at the horizontal mid-plane of the test section. To stabilize the laminar–turbulent transition of the boundary layer, a sandpaper trip was attached at 2.8 cm from the leading edge of the plate. Further control of the leading-edge stagnation point on the flat plate can be effected by a trailing-edge flap. Smoke, for flow visualization and study of shear flow dispersion, could be injected through slits in the wall and into the free stream. Some of these aspects of the experiment are described in Piomelli *et al.* (1993). The free-stream velocity, held constant at 1.8 m s^{-1}, was continuously monitored by a pitot-static tube/electronic manometer system, and the free-stream temperature was monitored with a thermocouple. The measurements were made at a downstream position of 3.6 m from the leading edge of the plate where the Reynolds number, based on momentum thickness, θ, was $R_\theta \approx 1070$ and was $Re_\tau \approx 543$ based on the friction velocity and boundary layer thickness. At this location, the boundary layer thickness, δ, was approximately 9.9 cm, and the friction velocity, determined by a Clauser fit to the Coles' (1962) expression ($U^+ = 2.44 \ln y^+ + 5.0$) for measured data in the logarithmic region, was $u_\tau = 0.089$ *m* s^{-1}. Here $U^+ \equiv \overline{U}/u_\tau$, $y^+ \equiv yu_\tau/\nu$, the overbar denotes time-averaged values, and y is the distance from and normal to the wall.

The nine-sensor hot-wire probe used in this investigation was operated in the constant-temperature mode with a 10 channel A.A. Lab Systems hot-wire anemometer system that has a frequency response that is flat up to about 4000 Hz for the flow conditions studied. The overheat ratio of the sensors was set at 1.2, which Vukoslavčević, Wallace & Balint (1991) have found gives adequate sensitivity while minimizing thermal cross-talk between neighbouring sensors. The voltage signals were digitized using the OPTIM Megadac 5017A data acquisition system that has a 250 kHz total throughput 12-bit A/D converter from three 8-channel sample and hold input cards. The acquisition system was interfaced with and controlled by a personal computer that was also used to transfer the data to a SUN host computer for post-processing and for permanent storage on tape. A sampling frequency of 1000 Hz was chosen so that, for positions close to the wall, the streamwise gradients, obtained by Taylor's hypothesis, would have a spatial resolution comparable to the cross-stream gradients, obtained by finite differencing, and that the Nyquist frequency of 500 Hz was above the highest frequencies with any significant energy in the velocity field. To ensure convergence of higher-order turbulence statistics, data were acquired continuously at each measurement location for 3 min. The nine-sensor hot-wire probe was calibrated before and after the measurements at each location in the boundary layer.

2.1. *The nine-sensor vorticity probe*

The design and performance of the nine-sensor probe for simultaneous measurement of velocity and vorticity vectors has been described in detail by Vukoslavčević *et al.* (1991). The probe consists of three arrays, each with three hot-wire sensors. Each sensor is inclined at approximately 45° to the mean flow direction, as shown in the sketch in figure 2, where the dimensions of the probe used in the present study are indicated. Tungsten sensor wires with a diameter of 2.5 μm are welded to the nickel plated tungsten prongs. The nominal length of each sensor is approximately 0.7 mm, giving a length to diameter ratio of 280. The data reduction method used and briefly summarized in Appendix A was developed by Marasli (see Marasli, Nguyen & Wallace 1993 for additional details) for multi-sensor probes of arbitrary number and orientation of the sensors.

The nine-sensor probe has a limited operational angle of attack cone, as has been discussed in detail by Vukoslavčević *et al.* (1991). When the instantaneous flow angle exceeds this cone angle (for this probe $> 20°$), the response equations may either fail to converge or converge to non-physical erroneous values. In view of this limitation, and since the probe's calibration was only performed for pitch and yaw angles between 20° and −20°, the data reduction program rejected solutions outside these calibration angles, thereby eliminating uncertainties due to extrapolation. Other experimental uncertainties, such as electronic noise on any of the sensor voltages, can have a significant effect on the nonlinear response equations and may also result in non-convergence of the solution scheme. In addition, Newton's solution method can fail when the initial guess of the solution is poor. In spite of these difficulties, the nine-sensor probe and the data reduction technique performed quite well in the present study, even for the closest measurements to the wall. The data loss is no more than 8% at $y^+ = 20$; this decreases to 0.5% at $y^+ = 35$. The effect of these data losses was determined to be negligible on both the statistical properties as well as the JPDFs. This was demonstrated by removing an additional 4% of the data at $y^+ = 20$ immediately before and after existing data loss segments, and observing that the results remain essentially unchanged.

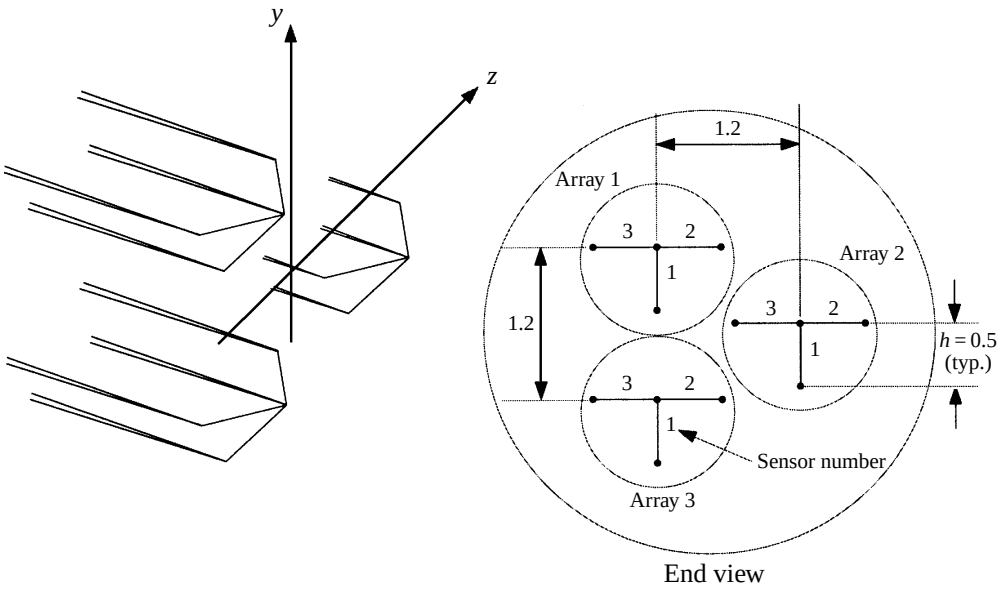

FIGURE 2. Schematic of the nine-sensor vorticity probe. Dimensions in mm.

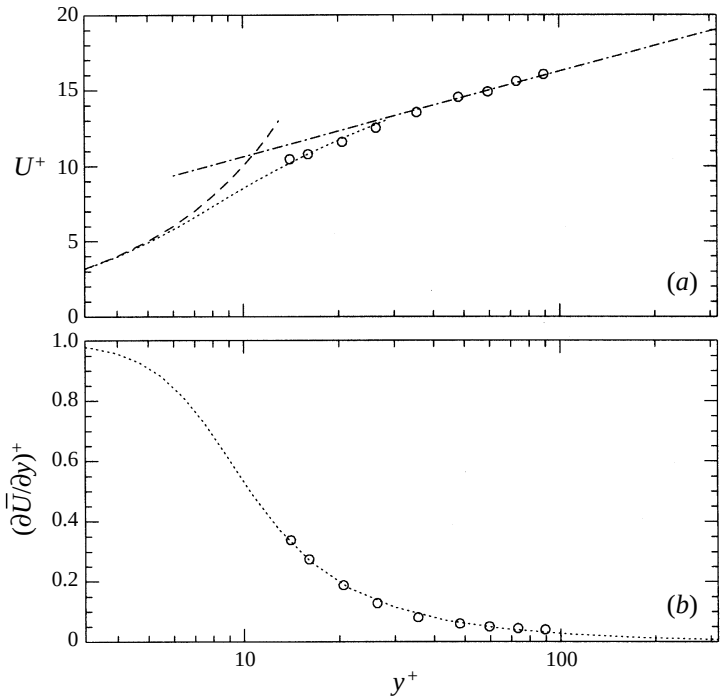

FIGURE 3. (*a*) Mean velocity profile, (*b*) mean shear profile: ○, present data; – – –, $U^+ = y^+$; ·····, Spalding (1961); —·—, Coles (1962).

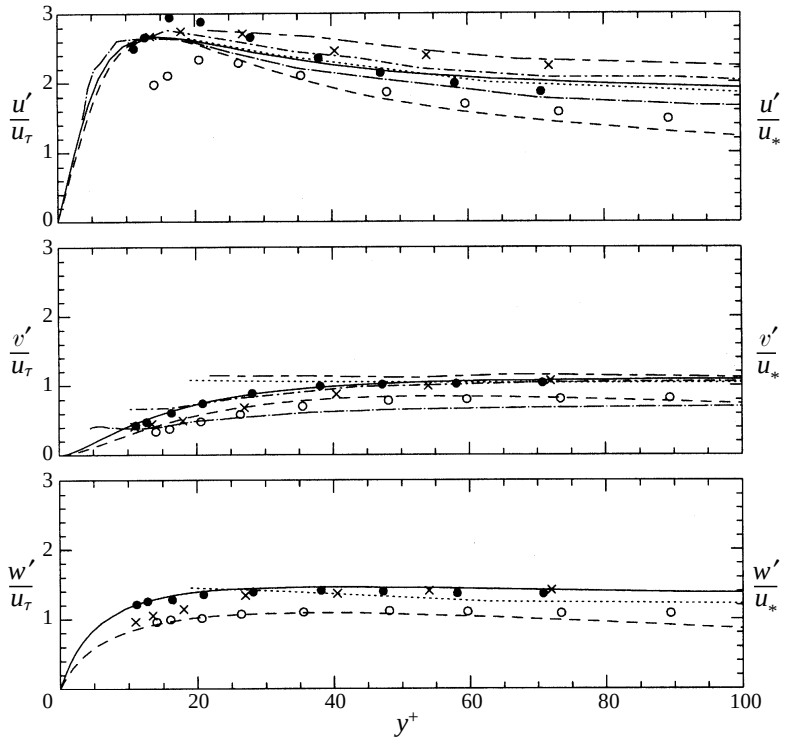

FIGURE 4. Effects of the scaling friction velocity on r.m.s. values; ○, present data at $R_\tau = 543$ scaled with u_τ, • and with an estimate of u_*; ×, Balint *et al.* (1991) at $Re_\tau = 1134$; ·····, Kastrinakis & Eckelmann (1983) at $Re_\tau = 545$; – – –, Kim *et al.* (1987) at $Re_\tau = 180$; —·—, Klewicki (1989) at $Re_\tau = 969$; ———, Spalart (1988) at $Re_\tau = 660$; —·—·—, Wei & Willmarth (1989) at $Re_\tau = 329$; and ——– ——, Wei & Willmarth (1989) at $Re_\tau = 3125$.

3. Statistical properties

In order to validate the quality of these data, a comparison of some statistical properties of the boundary layer to previously published experimental and direct numerical simulation (DNS) results at similar low Reynolds numbers will be made.

3.1. *Mean velocity*

The mean velocity profile is plotted in figure 3(*a*). The measurements in the buffer layer compare well with Spalding's (1961) empirical fit of a compilation of data from the literature and in the logarithmic layer with the Coles' (1962) empirical fit. The directly measured mean velocity gradient values, $(\partial\overline{U}/\partial y)^+ \equiv (\nu/u_\tau^2)\partial\overline{U}/\partial y$, are compared with the derivative of Spalding's fit (dotted line) in figure 3(*b*). The agreement is excellent.

3.2. *Moments of the velocity and vorticity components*

Most of the published data from the turbulent boundary layer wall region are scaled with u_τ and ν. The required friction velocity, u_τ, is usually approximated by the Clauser method, as described in § 2, or is determined from the direct measurements of the slope of the velocity profile in the linear sublayer ($y^+ \leqslant 7$). This latter method only can be achieved experimentally with hot wires by using very small single-sensor probes for low Reynolds number flows. The use of hot-wire probes near solid boundaries is complicated by free convection effects and heat losses from

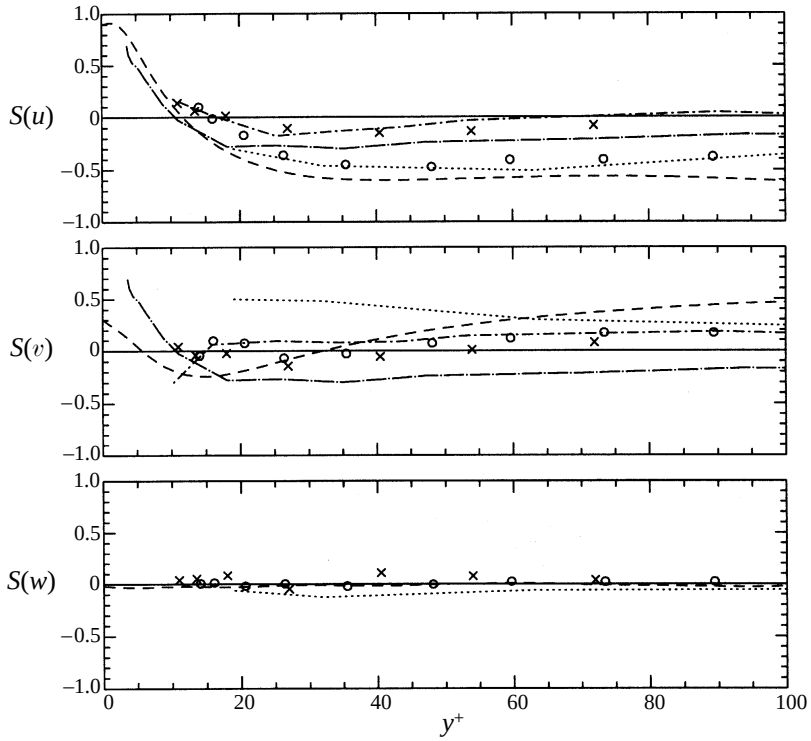

FIGURE 5. Skewness factors of the velocity components. Symbols as in figure 4.

the sensor to the wall. The probe used in this experiment, with a sensing diameter of approximately 5.6 Kolmogorov length scales, η, did not have sufficient spatial resolution for such a direct determination of the friction velocity. While numerical simulations (Spalart 1988; Kim, Moin & Moser 1987) used numerical grids with fine enough spatial resolutions near the wall to obtain a good direct estimate of the velocity gradient in the sublayer, experiments such as the present one and that of Balint *et al.* (1991) have relied on approximate values of u_τ from the Clauser method to scale the data.

Blackwelder & Haritonidis (1983) have shown that, over a Reynolds number range of $R_\theta = 1000$–$10\,000$, friction velocity values estimated from the Clauser fit of the velocity profile in the logarithmic layer ($2.44 \ln y^+ + 5.0$) are larger than those, which they denoted by u_*, obtained directly from the slope of the velocity profile in the linear viscous sublayer, with a ratio of the former to the latter varying between 1.08 and 1.20. Similarly, Kline *et al.* (1967) found the ratio u_τ/u_* to vary between about 1.08 and 1.13 for $R_\theta = 545$–2060, when u_τ was obtained from a fit to the logarithmic velocity profile, $2.44 \ln y^+ + 4.9$. Spalart (1988) also observed this effect for his lowest Reynolds number turbulent boundary layer DNS. This difference obviously affects the scaling of the fluctuating velocity and vorticity component r.m.s. values. The vorticity values are particularly affected because they are scaled with u_τ^2. A value of $u_*/U_\infty = 0.043$ for $Re_\tau = 1000$ can be taken from the tabulation of Blackwelder & Haritonidis (1983). When compared to the Clauser fit value of $u_\tau/U_\infty = 0.49$ for the present experiment, a ratio of $u_\tau/u_* = 1.14$ is obtained. This agrees fairly well with the values of this ratio found by Blackwelder & Haritonidis (1983) and by Kline *et al.* (1967) at similar values of R_θ. Thus it seems reasonable to use a value of

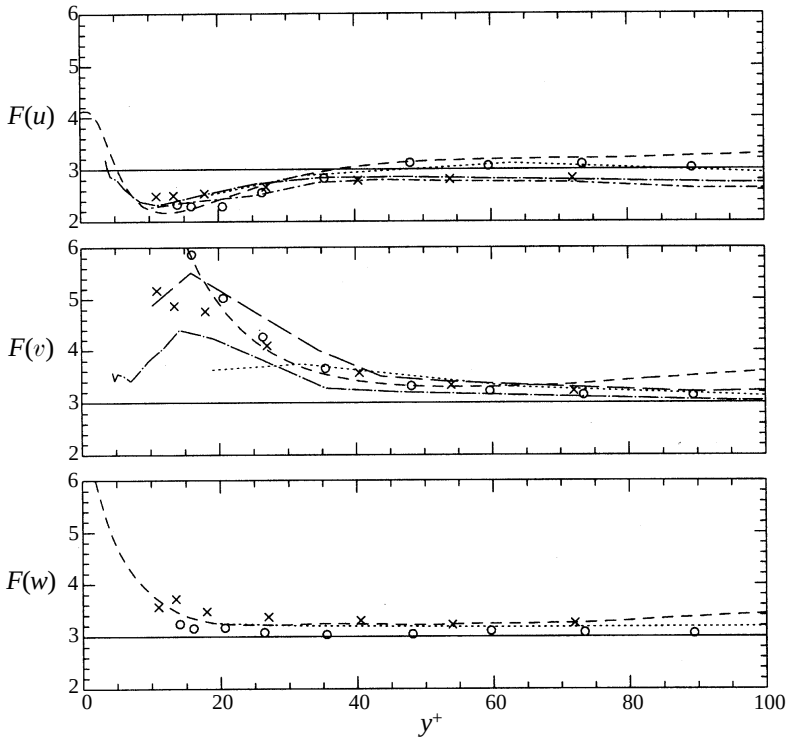

FIGURE 6. Flatness factors of the velocity components. Symbols as in figure 4.

u_*, estimated by taking Blackwelder & Haritonidis' (1983) value of u_*/U_∞, in order to observe the range of uncertainty, due to the difference between u_τ and u_*, when comparing the normalized data to DNS results.

The r.m.s. (denoted by $'$) distributions of the fluctuating velocity components are shown in figure 4, with open circles representing the present measurements scaled with u_τ, and the filled circles representing the same data scaled with u_*. The values of y^+ for these two non-dimensionalizations of the data are, of course, also determined using u_τ and u_*, respectively. Also compared in this figure are the measurements of Balint *et al.* (1991), Klewicki (1989), Wei & Willmarth (1989), Kastrinakis & Eckelmann (1983) and the DNS values of Kim *et al.* (1987) and Spalart (1988). It is evident that, when the present r.m.s. values are scaled with u_*, they compare very well with the results of Spalart (1988) at a similar R_τ except that, between $15 < y^+ < 30$, u'/u_* from our experiment is somewhat larger. The results of Kim *et al.* 1987 have lower magnitudes, reflecting the lower Reynolds number of their simulation.

The skewness factor distributions of the velocity components are plotted in figure 5. These distributions and those for the flatness factor, of course, are not affected by the choice of friction velocity for scaling. The skewness factors of the fluctuating streamwise velocity component, $S(u)$, are negative at measurement locations of this study and compare very well to the results of Kim *et al.* (1987) and Kastrinakis & Eckelmann (1983). The skewness factor distribution of the wall normal velocity component, $S(v)$, tends to be slightly negative between $20 \leqslant y^+ \leqslant 40$, beyond which it becomes positive. This is consistent with the results of Balint *et al.* (1991) and Kim *et al.* (1987). The skewness factor of the spanwise velocity fluctuations, $S(w)$,

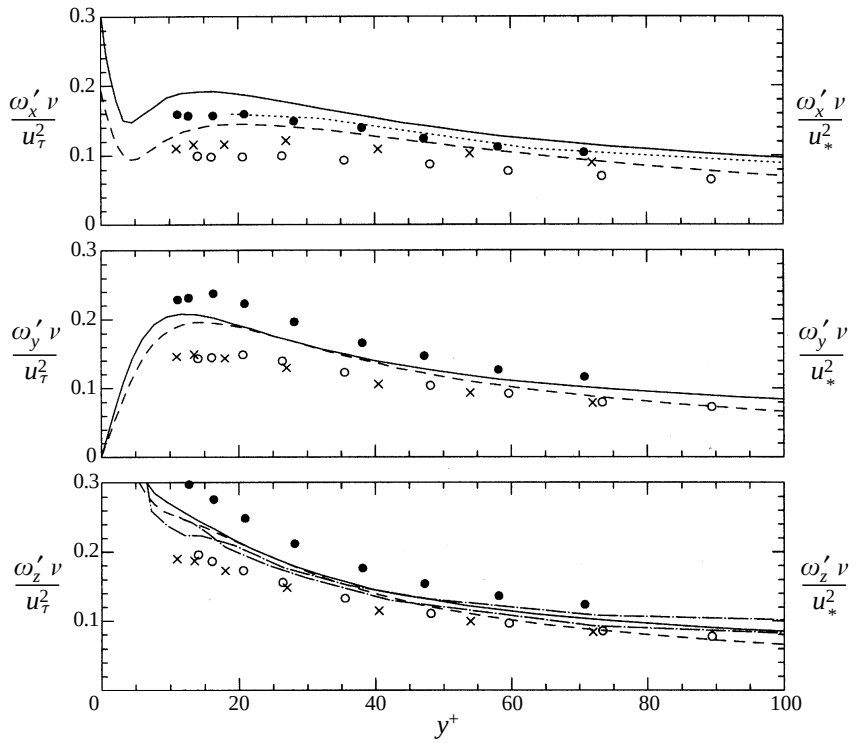

FIGURE 7. Effects of the scaling friction velocity on the vorticity r.m.s. Symbols as figure 4 except there are no data from Wei & Willmarth (1989).

is very nearly zero as is required by symmetry for this boundary layer, which is two-dimensional in the mean.

The flatness factor distributions of the velocity fluctuations are shown in figure 6. The horizontal solid line in the plot indicates the flatness factor value of 3.0 for a Gaussian random variable. These measured flatness factor values for all three velocity components compare very well with the results of others, most particularly with the DNS of Kim *et al.* (1987).

The r.m.s. distribution of the fluctuating vorticity components is shown in figure 7. When our ω_x' values are scaled with u_*^2, they fall between the values of Spalart (1988) and those of Kim *et al.* (1987). Our measurements of ω_y'/u_*^2 and ω_z'/u_*^2 are somewhat higher than those of Kim *et al.* (1987) and of Spalart (1988). As noted above, obviously the uncertainty in experimentally determining the friction velocity, because it is squared, has a strong affect on these vorticity component r.m.s. comparisons. The skewness and flatness factors for the fluctuating vorticity components are shown in figures 8 and 9, respectively. Our results for these higher-order moments are reasonably consistent with the results of other investigators. In particular, the values of $S(\omega_x)$ and $S(\omega_y)$ are nearly zero, as required by the symmetry of the flow.

Viewed as a whole, the comparisons in this section indicate that the velocity and vorticity component values measured in this experiment are of reasonably good accuracy, and thus they can be relied upon for the joint probability density function analysis to follow below.

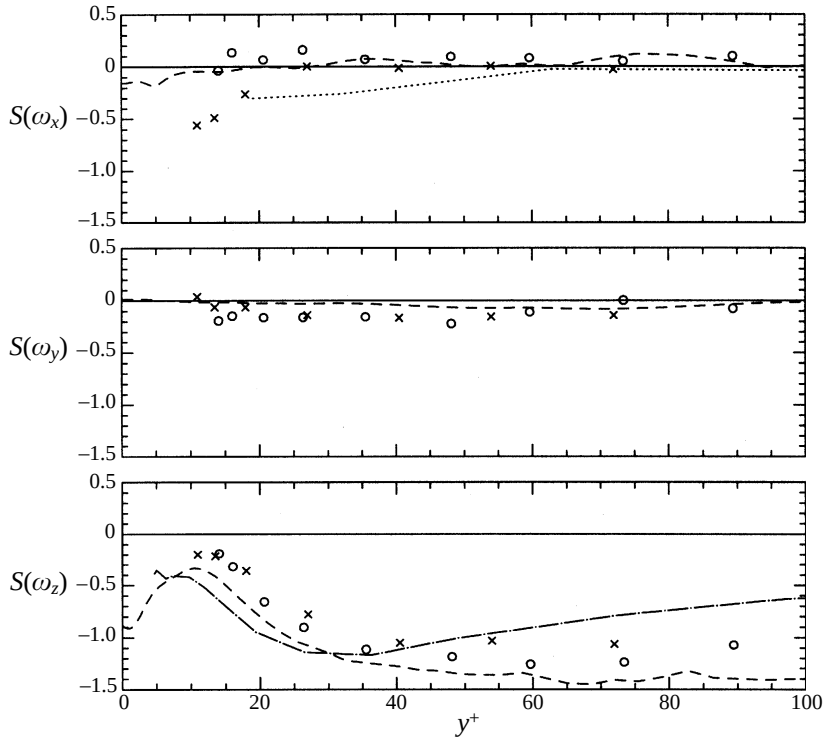

FIGURE 8. Skewness factors of the vorticity components. Symbols as in figure 7.

4. Joint probability density function analysis

Quadrant analysis of the Reynolds shear stress covariance, $\overline{uv}$, developed independently by Wallace, Eckelmann & Brodkey (1972) and Willmarth & Lu (1972), resulted in a greater understanding of the physical processes underlying turbulent momentum transport. An extension of quadrant analysis was carried out by Wallace & Brodkey (1977), who made a detailed analysis of the Reynolds shear stress in a turbulent channel flow by determining its joint probability density function (JPDF), $P(u,v)$, where

$$\overline{uv} = \iint_{-\infty}^{\infty} uvP(u,v)\mathrm{d}u\mathrm{d}v. \tag{4.1}$$

This integral of the covariance integrand, $uvP(u,v)$, over a differential area $\mathrm{d}u\mathrm{d}v$ of the (u,v)-plane, represents the contribution of that particular simultaneous combination of sign and magnitude of u and v to the Reynolds shear stress covariance, $\overline{uv}$. By plotting contours of the $P(u,v)$ JPDFs as well as of the covariance integrands, $uvP(u,v)$, Wallace & Brodkey (1977) showed that sweep, or quadrant 4 (Q4: $+u,-v$) events, are the dominant contributors to the Reynolds shear stress very near the wall for $y^+ < 15$. Farther from the wall, ejections, or quadrant 2 (Q2: $-u,+v$) events, become the major contributors. Plots of $P(u,v)$ and $uvP(u,v)$ for the present boundary layer experiment are shown in figure (10) for $y^+ = 20, 35$ and 89, where u and v are made non-dimensional by u_τ. The shapes of these plots and the location of their maxima compare well to those of Wallace & Brodkey (1977) for similar y^+ locations in their channel flow. The covariance integrand contour plots show the dominant

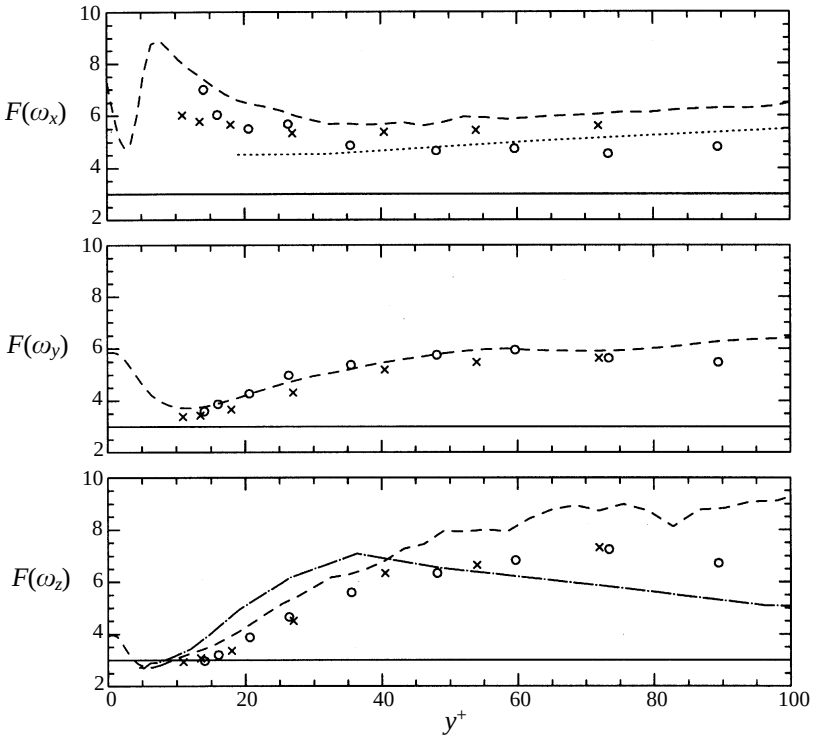

FIGURE 9. Flatness factors of the vorticity components. Symbols as in figure 7.

contributions of quadrants Q2 and Q4 to the $\overline{uv}$ covariance. This type of JPDF and covariance integrand analysis will be applied below to covariances of various terms which describe aspects of the structure and dynamics of the vorticity field. All the JPDF and covariance integrand figures in this investigation have been plotted using matrices of 100 $\times$ 100 bins.

4.1. *Vorticity–vorticity covariances*

The transport equation for the mean fluctuating enstrophy, $\zeta \equiv \frac{1}{2}\overline{\omega_i\omega_i}$, has been used to good effect in two-equation modelling by Robinson, Harris & Hassan (1995) and by Gorski & Bernard (1996) as a surrogate for the dissipation rate, ϵ, transport equation. The ϵ-equation is notoriously difficult to model near walls in bounded flows, and it is often modelled like the turbulent kinetic energy, resulting in unphysical model behaviour. The fluctuating vorticity component covariance, $\overline{\omega_x\omega_y}$, when coupled with the mean velocity gradient, $\partial\overline{U}/\partial y$, forms one of the largest production terms in the ζ-equation (see Gorski et al. 1994). Here the total vorticity covariances, $\overline{\Omega_i\Omega_j}$, are studied to obtain a physical picture of the spatial orientation of the vorticity filaments that contribute most to them.

Indications of the orientations of projections of vorticity filaments on the (x, y)-plane of the boundary layer are given by the $P(\Omega_x, \Omega_y)$ JPDF contours seen in figure 11(a), where Ω_x and Ω_y are made non-dimensional by ν/u_τ^2. Here, and in other figures, vorticity and velocity gradient components are non-dimensionalized by this viscous time scale. The shapes of the contours indicate that the more probable orientation of vorticity filaments is one of inclination downstream, at an angle to the wall that may vary along the filament. These filaments may be configured as

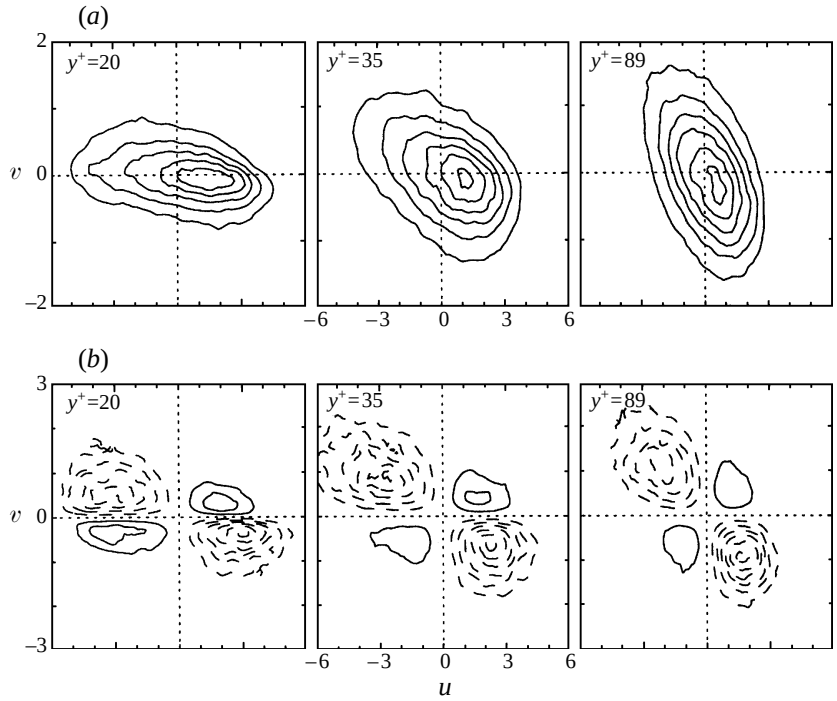

FIGURE 10. (*a*) JPDFs and (*b*) covariance integrands of u and v, non-dimensionalized by u_τ. Contour increments (for $y^+ = 20$, 35 and 89, respectively) are (*a*) 3.1×10^{-2}, 2.4×10^{-2}, 2.4×10^{-2} and (*b*) 1.6×10^{-4}, 2.1×10^{-4}, 2.1×10^{-4}. The outer contours are one increment above zero. Solid contour lines are positive and dashed contour lines are negative in this and the following figures.

single elements with either sense of rotation, as illustrated by the solid arrows in figure 12, or in counter-rotating pairs, as illustrated by the shaded arrow loop that indicates one possible configuration for such counter-rotating pairs: a hairpin shape. There are several other possible configurations of these counter-rotating pairs, but the single-point vorticity component data of this experiment do not permit distinguishing between the variety of these possibilities, nor do they permit the determination of how these vorticity filaments are clustered in space. However, they do provide information about the probability of occurrence of angles of inclination of the projections of the vorticity filaments on the three coordinate planes.

Analagous to the Reynolds shear stress covariance, $\overline{uv}$, for the velocity vector fluctuations, the covariance $\overline{\Omega_x \Omega_y}$ is the correlation of the streamwise and wall normal components of the vorticity vector. The JPDFs in figure 11(*a*) clearly indicate a preference for like-sign Ω_x and Ω_y to occur at the same time. This results in a positive covariance, $\overline{\Omega_x \Omega_y}$, with values of the correlation coefficient of 0.30, 0.31 and 0.22 for the three y^+ (20, 35 and 89, respectively) positions shown.

The $\Omega_x \Omega_y P(\Omega_x, \Omega_y)$ covariance integrand plots of figure 11(*b*) show even more clearly that the covariance is positive because of the dominance of the contributions from quadrants Q1 $(+\Omega_x, +\Omega_y)$ and Q3 $(-\Omega_x, -\Omega_y)$. The orientation of segments of vorticity filaments with projections on the (x, y)-plane making angles with the positive x-axis of $\theta \equiv \tan^{-1}(\Omega_y/\Omega_x)$ can be inferred from the peaks in these covariance integrand Q1 and Q3 quadrants. These vorticity filament segments, with angles of inclination θ of about 58° , 48° and 48° (for Q1) and −118°, −136° and

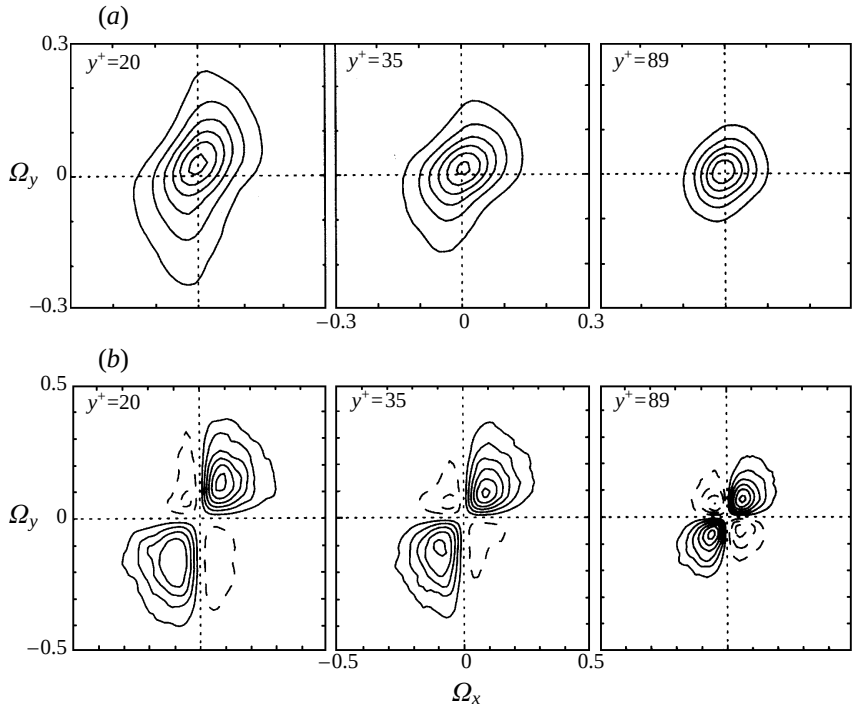

FIGURE 11. (*a*) JPDFs and (*b*) covariance integrands of Ω_x and Ω_y, non-dimensionalized by ν/u_τ^2. All vorticity and velocity gradients are normalized by this time scale here and in the following figures. Contour increments (for $y^+ = 20$, 35 and 89, respectively) are (*a*) 3.3, 4.5, 9.0 and (*b*) 3.4×10^{-6}, 2.9×10^{-6}, 1.4×10^{-6}. The outer contours are one increment above zero.

$-137°$ (for Q3), make the greatest contribution to the $\overline{\Omega_x \Omega_y}$ covariance at $y^+ = 20$, 35 and 89, respectively. Thus these vorticity filaments, dominant in this limited sense, are inclined at decreasing angles to the streamwise direction with increasing distance from the wall moving from the buffer to the logarithmic layer. These angles of inclination depend somewhat on the matrix size, which is limited by the sample size, used for the JPDFs and covariance integrands, and the accuracy with which they have been determined is not great. The worst possible angle error for this matrix bin size is about $\pm 5°$. However, the trends with wall distance can be discerned and are independent of the number of bins used in the JPDF and covariance integrand matrices. This decreasing angle of inclination is qualitatively consistent with observations of Bernard, Thomas & Handler (1993) who plotted the projections on the (x, y)-plane of the vorticity vectors at the centre of the set of quasi-streamwise vorticies that they identified in a $R_\tau = 125$ channel flow DNS.

It is apparent from the somewhat triangular shaped $P(\Omega_x, \Omega_z)$ JPDFs at $y^+ = 20$ and 35 in figure 13 that, in the buffer layer and lower part of the logarithmic layer, the vorticity filaments usually do not have much streamwise orientation when the spanwise vorticity, Ω_z, is large and negative (i.e. of the same sign as the mean shear). Conversely, the largest values of Ω_x occur when Ω_z is nearly zero. At $y^+ = 20$ the largest contribution to the covariance $\overline{\Omega_x \Omega_z}$ (the peaks in the covariance integrand contours) come from segments of vorticity filaments with projections on the (x, z)-plane forming angles $\gamma \equiv \tan^{-1}(\Omega_x/\Omega_z)$ of about $\pm 16°$ with the negative spanwise

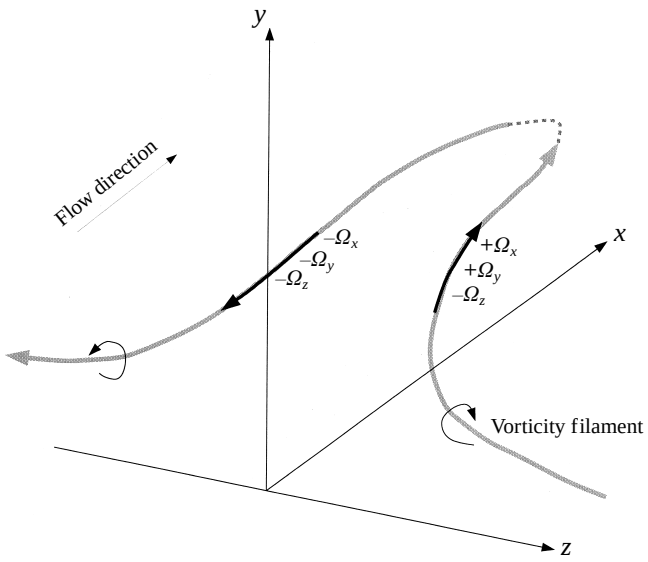

FIGURE 12. Models of inclined vorticity filaments.

z-axis. This indicates that these vorticity filaments are oriented primarily in the negative spanwise direction in the buffer layer. However, at $y^+ = 35$ this angle increases to about $\pm 27^\circ$, indicating that the vorticity filaments rotate toward the streamwise direction with increasing distance from the wall. At $y^+ = 89$ this angle increases further to about $\pm 42^\circ$.

The largest contribution to the covariance $\overline{\Omega_y \Omega_z}$ at $y^+ = 20$, as inferred from figure 14, comes from vorticity filament segments with projections on the (y, z)-plane forming angles $\phi \equiv \tan^{-1}(\Omega_y/\Omega_z)$ of about $\pm 27^\circ$ with the negative spanwise z-axis. This indicates that, at this location, these filaments that contribute most to the covariance already have significantly rotated from the negative spanwise to the normal direction. At $y^+ = 35$ and 89 this angle increases to about $\pm 35^\circ$ and $\pm 37^\circ$, respectively.

These patterns of orientation of the vorticity filaments in the (x, z)- and (y, z)-planes are also qualitatively consistent with the observations of Bernard *et al.* (1993). They note that, although they can identify obvious quasi-streamwise vortices in the (y, z)-planes of their DNS, close to the wall the vorticity vectors at the centres of these vortices often have larger Ω_y and Ω_z components than Ω_x. Brooke & Hanratty (1993) and Miyake & Tsujimoto (1996) have found that projections of the vorticity filament lines on the cross-stream (y, z) plane passing through the cores of detected quasi-streamwise vortices are almost vertical in their respective simulations of turbulent channel flows.

Sketches of the projections of these vorticity filaments making the largest contribution to the covariances $\overline{\Omega_x \Omega_y}$, $\overline{\Omega_x \Omega_z}$ and $\overline{\Omega_y \Omega_z}$ are shown in figure 15. Note that these three views are *not* the projections of segments of a *single* manifestation of a three-dimensional filament. Such information cannot be obtained from JPDFs of two vorticity components. Each of these projected views may correspond to an ensemble of *different* orientations in the other two planes of the vorticity filaments that most contribute to the vorticity component covariances.

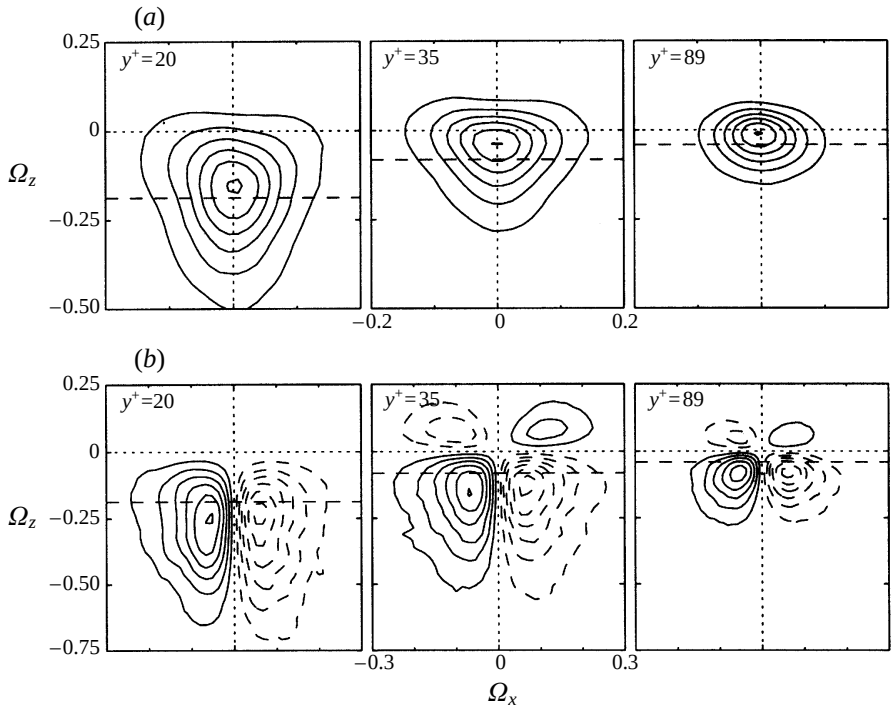

FIGURE 13. (*a*) JPDFs and (*b*) covariance integrands of Ω_x and Ω_z. Dashed lines (– – –) indicate $\overline{\Omega_z}$ at each y^+ position. Contour (for $y^+ = 20$, 35 and 89, respectively) increments are (*a*) 2.6, 3.7, 8.0 and (*b*) 6.5×10^{-6}, 3.7×10^{-6}, 2.3×10^{-6}. The outer contours are one increment above zero.

4.2. *Vorticity–velocity gradient covariances*

The processes of vorticity filament stretching and compression, due to their reorientation by the velocity gradient field, are mathematically expressed by the first term (III) on the right-hand side in the vorticity transport equation (1.1). This term can be studied using the $P(\Omega_j, \partial U_i/\partial x_j)$ JPDFs and the covariance integrands, $\Omega_j(\partial U_i/\partial x_j)P(\Omega_j, (\partial U_i/\partial x_j))$. These same processes result in rates of gains or losses in the component parts of the enstrophy, as expressed in the first term (III) on the right-hand side of equation (1.2),

$$\underbrace{\Omega_i\Omega_j\frac{\partial U_i}{\partial x_j}}_{\text{III}} = \Omega_x\Omega_x\frac{\partial U}{\partial x} + \Omega_x\Omega_y\frac{\partial U}{\partial y} + \Omega_x\Omega_z\frac{\partial U}{\partial z}$$

$$+\Omega_y\Omega_x\frac{\partial V}{\partial x} + \Omega_y\Omega_y\frac{\partial V}{\partial y} + \Omega_y\Omega_z\frac{\partial V}{\partial z}$$

$$+\Omega_z\Omega_x\frac{\partial W}{\partial x} + \Omega_z\Omega_y\frac{\partial W}{\partial y} + \Omega_z\Omega_z\frac{\partial W}{\partial z}. \tag{4.2}$$

The sum of each row of terms on the right-hand side of equation (4.3) expresses the instantaneous time rate of change, due to stretching or compression of vorticity filaments, of the respective parts of the enstrophy: $\partial(\frac{1}{2}\Omega_x^2)/\partial t$, $\partial(\frac{1}{2}\Omega_y^2)/\partial t$,

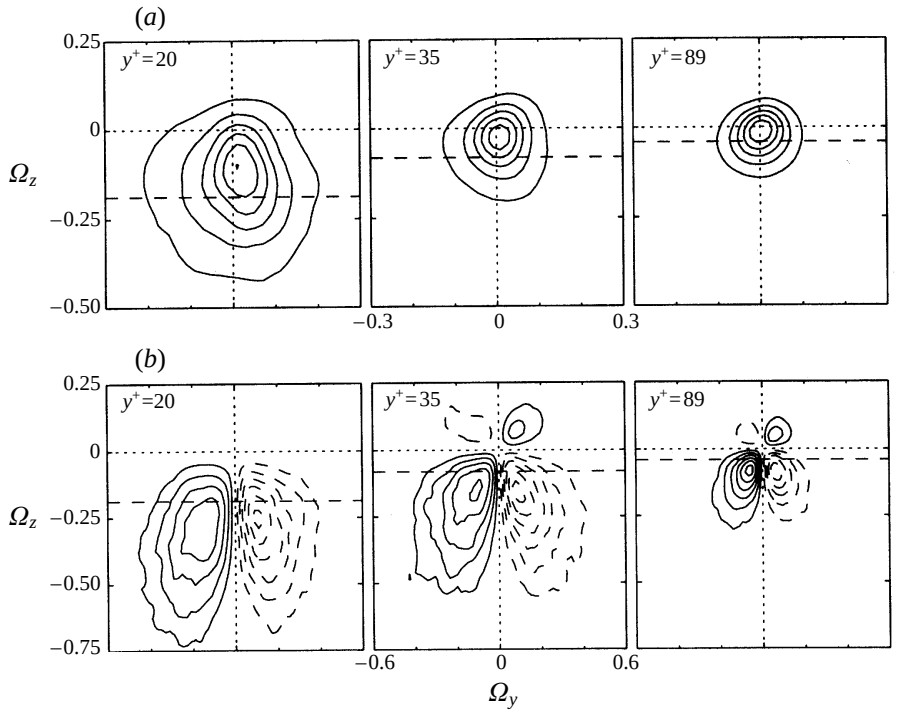

FIGURE 14. (*a*) JPDFs and (*b*) covariance integrands of Ω_y and Ω_z. Dashed lines (– – –) indicate $\overline{\Omega_z}$ at each y^+ position. Contour increments (for $y^+ = 20$, 35 and 89, respectively) are (*a*) 1.8, 4.4, 8.1 and (*b*) 1.0×10^{-5}, 4.4×10^{-6}, 3.0×10^{-6}. The outer contours are one increment above zero.

$\partial(\frac{1}{2}\Omega_z^2)/\partial t$. The covariances $\overline{\Omega_i \Omega_j \partial U_i/\partial x_j}$ can be most usefully investigated using joint probability analysis by grouping the variables as $P(\Omega_i, \Omega_j \partial U_i/\partial x_j)$ and $\Omega_i \Omega_j \partial U_i/\partial x_j P(\Omega_i, \Omega_j \partial U_i/\partial x_j)$. That this is the most rational grouping can be seen by expressing the left-hand side of equation (4.3) in vector form, i.e. $\boldsymbol{\Omega} \cdot (\boldsymbol{\Omega} \cdot \nabla \boldsymbol{V})$.

Before looking at the details of the stretching/compression processes by means of the JPDFs and covariance integrands shown and discussed below in §§ 4.2.1–4.2.3, it is worthwhile to look at the net effects of these processes. A measure of the net rates of change in the magnitudes of the vorticity components due to stretching and compression is given by the averages of the terms on the right-hand side of equation (4.3), i.e. the covariances $\overline{\Omega_i \Omega_j \partial U_i/\partial x_j}$. Non-dimensional values of these nine covariances for all of the measurement positions are shown in figure 16. It is evident that, on balance, stretching dominates somewhat over compression of vorticity filaments. The principal covariance producing a large positive rate of change of $(\pm\Omega_x)^2$ by stretching in the buffer layer is $\overline{\Omega_x \Omega_y \partial U/\partial y}$, and for $(\pm\Omega_z)^2$ it is $\overline{\Omega_z \Omega_z \partial W/\partial z}$. The principal covariance resulting in a large negative rate of change of $(\pm\Omega_x)^2$ by compression in the buffer layer is $\overline{\Omega_x \Omega_z \partial U/\partial z}$, and for $(\pm\Omega_z)^2$ it is $\overline{\Omega_z \Omega_y \partial W/\partial y}$. The balance of stretching and compression results in a net rate of change of the $(\pm\Omega_y)^2$ part of the enstrophy that is very nearly zero. This is due to a combination of smaller magnitudes of the covariances and, for the case of $\overline{\Omega_y \Omega_y \partial V/\partial y}$, approximate balance between vorticity filament stretching and compression as described in Appendix B.

It should be noted that Brooke & Hanratty (1993) have pointed out that the gradients product $\partial U/\partial z \cdot \partial U/\partial y$ appears twice, with opposite signs, in both the $\Omega_y \partial U/\partial y$ and $\Omega_z \partial U/\partial z$ stretching/compression terms of the transport equation for

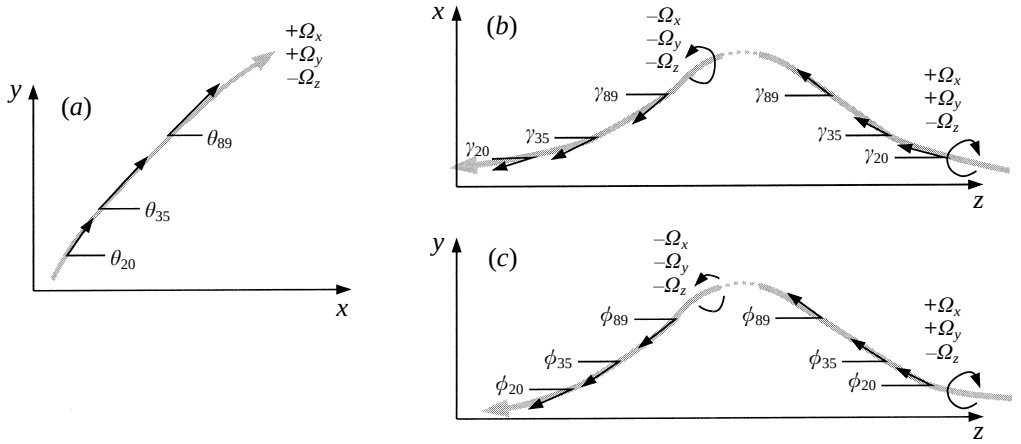

FIGURE 15. Projections of vorticity filament segments making the largest contributions to $\overline{\Omega_x\Omega_y}$, $\overline{\Omega_x\Omega_z}$ and $\overline{\Omega_y\Omega_z}$ at $y^+ = 20$, 35 and 89. (*a*) Projection on (x, y)-plane where $\theta \equiv \tan^{-1}(\Omega_y/\Omega_x)$: $\theta_{20} \approx 58°(\text{or} - 118°)$ at $y^+ = 20$, $\theta_{35} \approx 48°$ (or $-136°$) at $y^+ = 35$ and $\theta_{89} \approx 48°$ (or $-137°$) at $y^+ = 89$. (*b*) Projection on (x, z)-plane where $\gamma \equiv \tan^{-1}(\Omega_x/\Omega_z)$: $\gamma_{20} \approx \pm 16°$, $\gamma_{35} \approx \pm 27°$ and $\gamma_{89} \approx \pm 42°$. (*c*) Projection on (y, z)-plane where $\phi \equiv \tan^{-1}(\Omega_y/\Omega_z)$: $\phi_{20} \approx \pm 27°$, $\phi_{35} \approx \pm 35°$ and $\phi_{89} \approx \pm 37°$.

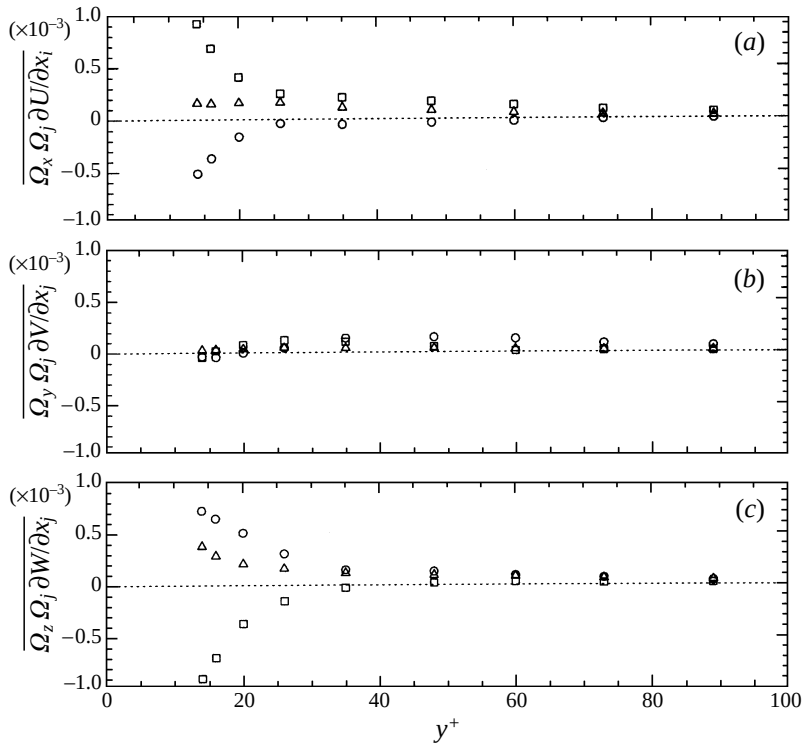

FIGURE 16. Distribution of $\overline{\Omega_i\Omega_j\partial U_i/\partial x_j}$ components across the boundary layer. (*a*) Contributors to $\overline{\Omega_x^2}$: △, $\overline{\Omega_x\Omega_x\partial U/\partial x}$; □, $\overline{\Omega_x\Omega_y\partial U/\partial y}$; ○, $\overline{\Omega_x\Omega_z\partial U/\partial z}$ (*b*) contributors to $\overline{\Omega_y^2}$: △, $\overline{\Omega_y\Omega_x\partial V/\partial x}$; □, $\overline{\Omega_y\Omega_y\partial V/\partial y}$; ○, $\overline{\Omega_y\Omega_z\partial V/\partial z}$ (*c*) contributors to $\overline{\Omega_z^2}$: △, $\overline{\Omega_z\Omega_x\partial W/\partial x}$; □, $\overline{\Omega_z\Omega_y\partial W/\partial y}$, ○, $\overline{\Omega_z\Omega_z\partial W/\partial z}$.

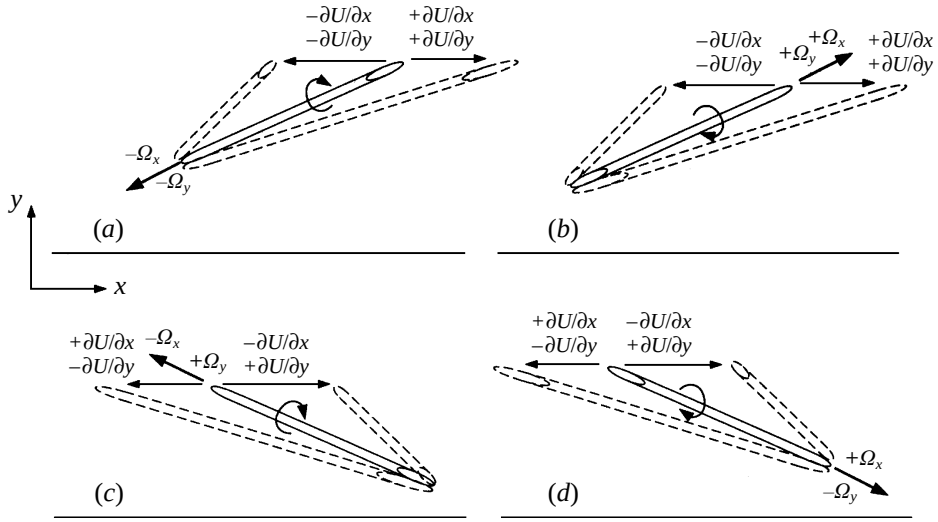

	Stretching	Figure 19	20	21	22	Compression	Figure 19	20	21	22
(*a*)	$-\Omega_x\ -\Omega_y\ +\frac{\partial U}{\partial x}$ or $+\frac{\partial U}{\partial y}$	Q2	Q3	Q2	Q3	$-\Omega_x\ -\Omega_y\ -\frac{\partial U}{\partial x}$ or $-\frac{\partial U}{\partial y}$	Q3	Q2	Q3	Q2
(*b*)	$+\Omega_x\ +\Omega_y\ +\frac{\partial U}{\partial x}$ or $+\frac{\partial U}{\partial y}$	Q1	Q1	Q1	Q1	$+\Omega_x\ +\Omega_y\ -\frac{\partial U}{\partial x}$ or $-\frac{\partial U}{\partial y}$	Q4	Q4	Q4	Q4
(*c*)	$-\Omega_x\ +\Omega_y\ +\frac{\partial U}{\partial x}$ or $-\frac{\partial U}{\partial y}$	Q2	Q3	Q4	Q3	$-\Omega_x\ +\Omega_y\ -\frac{\partial U}{\partial x}$ or $+\frac{\partial U}{\partial y}$	Q3	Q2	Q1	Q2
(*d*)	$+\Omega_x\ -\Omega_y\ +\frac{\partial U}{\partial x}$ or $-\frac{\partial U}{\partial y}$	Q1	Q1	Q3	Q1	$+\Omega_x\ -\Omega_y\ -\frac{\partial U}{\partial x}$ or $+\frac{\partial U}{\partial y}$	Q4	Q4	Q2	Q4

FIGURE 17. Set of possible orientations of projections of vorticity filaments on the (x, y)-plane being strained by $\pm\partial U/\partial x$ and $\pm\partial U/\partial y$ velocity gradients that change $\pm\Omega_x$.

streamwise vorticity. This has implications for the net balance of stretching and compression represented by the enstrophy covariance terms plotted in figure 16. For example, the product $\Omega_x\partial U/\partial z \cdot \partial U/\partial y$ appears, with opposite sign, respectively in the terms $\Omega_x\Omega_y\partial U/\partial y$ and $\Omega_x\Omega_z\partial U/\partial z$ in the first row of equation (4.3). Thus, these parts of these two terms, with the same magnitudes but opposite signs, cancel each other on average and contribute nothing to the net rate of change of $(\pm\Omega_x)^2$. Only the respective parts of the terms given by the products $\Omega_x\partial W/\partial x \cdot \partial U/\partial y$ and $\Omega_x\partial V/\partial x \cdot \partial V/\partial z$ contribute to the net imbalance between stretching and compression which results in the increase of $(\pm\Omega_x)^2$. The same thing can be said for the $\Omega_y\partial V/\partial z \cdot \partial V/\partial x$ product that appears, with opposite sign, in the terms $\Omega_y\Omega_x\partial V/\partial x$ and $\Omega_y\Omega_z\partial V/\partial z$ in the second row and for the $\Omega_z\partial W/\partial y \cdot \partial W/\partial x$ product that appears, with opposite sign, in the terms $\Omega_z\Omega_x\partial W/\partial x$ and $\Omega_z\Omega_y\partial W/\partial y$ in the third row.

4.2.1. Ω_x^2 *rates of change by vorticity filament stretching/compression*

The rate of change of Ω_x due to the reorientation by the velocity gradient field of arbitrarily oriented vorticity filaments is given by the sum of the terms $\Omega_x\partial U/\partial x + \Omega_y\partial U/\partial y + \Omega_z\partial U/\partial z$ in the x-component of equation (1.1). Likewise, the rate of change of the Ω_x part of the enstrophy, $\partial(\frac{1}{2}\Omega_x^2)/\partial t$, due to this reorientation is given by the sum of the terms $\Omega_x\Omega_x\partial U/\partial x + \Omega_x\Omega_y\partial U/\partial y + \Omega_x\Omega_z\partial U/\partial z$ in equations (1.2) and (4.3). How the $\partial U/\partial x$, $\partial U/\partial y$ and $\partial U/\partial z$ velocity gradients reorient a vorticity filament, thereby stretching or compressing it and thus changing the magnitude of

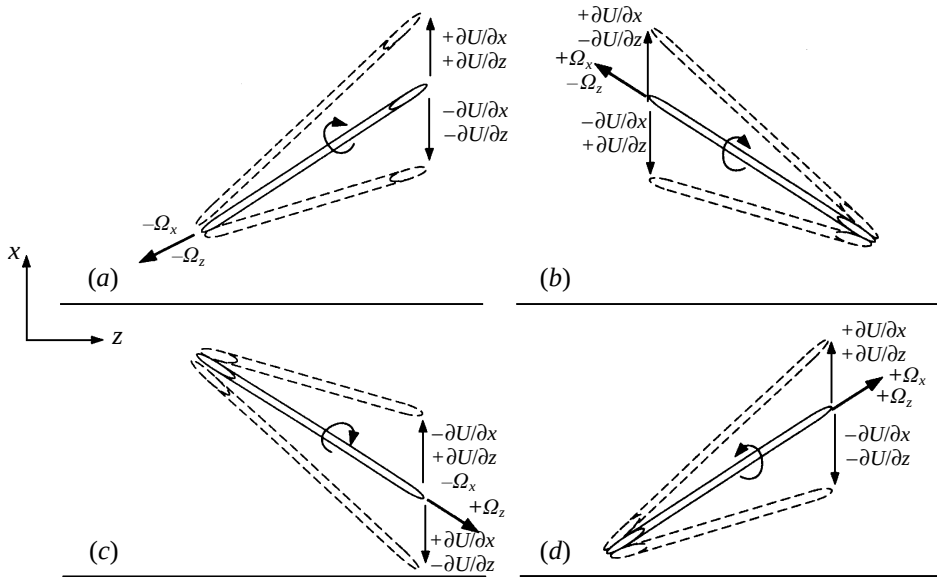

	Stretching	Figure 19	20	23	24	Compression	Figure 19	20	23	24
(*a*)	$-\Omega_x\ -\Omega_z\ +\frac{\partial U}{\partial x}$ or $+\frac{\partial U}{\partial z}$	Q2	Q3	Q2	Q3	$-\Omega_x\ -\Omega_z\ -\frac{\partial U}{\partial x}$ or $-\frac{\partial U}{\partial z}$	Q3	Q2	Q3	Q2
(*b*)	$+\Omega_x\ -\Omega_z\ +\frac{\partial U}{\partial x}$ or $-\frac{\partial U}{\partial z}$	Q1	Q1	Q3	Q1	$+\Omega_x\ -\Omega_z\ -\frac{\partial U}{\partial x}$ or $+\frac{\partial U}{\partial z}$	Q4	Q4	Q2	Q4
(*c*)	$-\Omega_x\ +\Omega_z\ +\frac{\partial U}{\partial x}$ or $-\frac{\partial U}{\partial z}$	Q2	Q3	Q4	Q3	$-\Omega_x\ +\Omega_z\ -\frac{\partial U}{\partial x}$ or $+\frac{\partial U}{\partial z}$	Q3	Q2	Q1	Q2
(*d*)	$+\Omega_x\ +\Omega_z\ +\frac{\partial U}{\partial x}$ or $+\frac{\partial U}{\partial z}$	Q1	Q1	Q1	Q1	$+\Omega_x\ +\Omega_z\ -\frac{\partial U}{\partial x}$ or $-\frac{\partial U}{\partial z}$	Q4	Q4	Q4	Q4

FIGURE 18. Set of possible orientations of projections of vorticity filaments on the (x, z)-plane being strained by $\pm\partial U/\partial x$ and $\pm\partial U/\partial z$ velocity gradients that change $\pm\Omega_x$.

its Ω_x vorticity component, is schematically illustrated in figures 17 and 18. The projection of an arbitrarily oriented vorticity filament on the (x, y)- and (x, z)-planes respectively, with each of the possible sign combinations of $\pm\Omega_x$ and $\pm\Omega_y$ or $\pm\Omega_z$, is stretched or compressed by the straining action of the velocity gradients shown. In figure 17, it is apparent that $\partial U/\partial x$ or $\partial U/\partial y$ strain has the effect, depending on the sign of the gradient and on the sign of Ω_y, of increasing or decreasing $\pm\Omega_x$. Likewise, in figure 18 the action of $\partial U/\partial x$ or $\partial U/\partial z$ increases or decreases $\pm\Omega_x$ depending on the sign of these gradients and on the sign of Ω_z.

Stretching increases of $\pm\Omega_x$ by $+\partial U/\partial x$ dominate compressive decreases by $-\partial U/\partial x$, especially near the wall. This is seen from the large positive contribution to the covariance $\overline{\Omega_x \partial U/\partial x}$ from quadrant Q1 $(+\partial U/\partial x, +\Omega_x)$ and negative contribution from Q2 $(+\partial U/\partial x, -\Omega_x)$ at $y^+ = 20$ in figure 19(*b*). The Q1 and Q2 fractional contributions to the covariance at $y^+ = 20$ are 8.88 and -7.73 compared to the 4.66 and -4.81 fractional contributions from Q3 and Q4. This dominance of stretching over compression is even more evident and easy to see in figure 20(*b*) which examines the $\Omega_x \Omega_x \partial U/\partial x$ term in equation (4.3). The rate of increase in $(+\Omega_x)^2$ enstrophy at $y^+ = 20$ by stretching given by the Q1 $(+\Omega_x, +\Omega_x \partial U/\partial x)$ and of $(-\Omega_x)^2$ by the Q3 $(-\Omega_x, -\Omega_x \partial U/\partial x)$ positive covariance integrand fractional contributions of 0.82 and 0.69 are about three times greater than the rate of compression losses given by the Q2 and Q4 negative fractional contributions of -0.24 and -0.26. The asymmetries

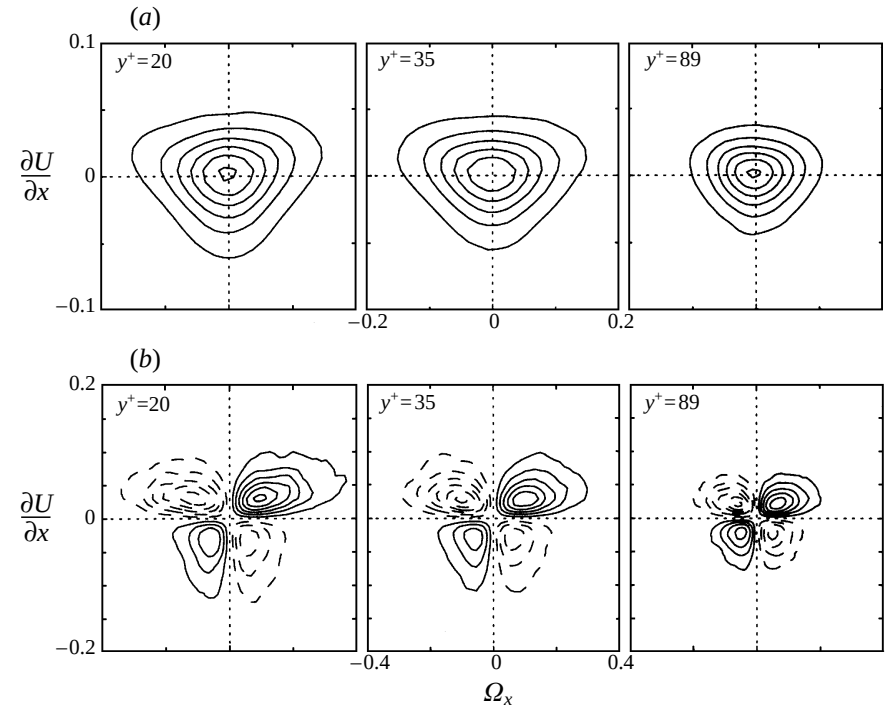

FIGURE 19. (*a*) JPDFs and (*b*) covariance integrands of Ω_x and $\partial U/\partial x$. Contour increments (for $y^+ = 20$, 35 and 89, respectively) are (*a*) 12.2, 13.3, 22.6 and (*b*) 1.1×10^{-6}, 1.1×10^{-6}, 4.3×10^{-7}. The outer contours are one increment above zero.

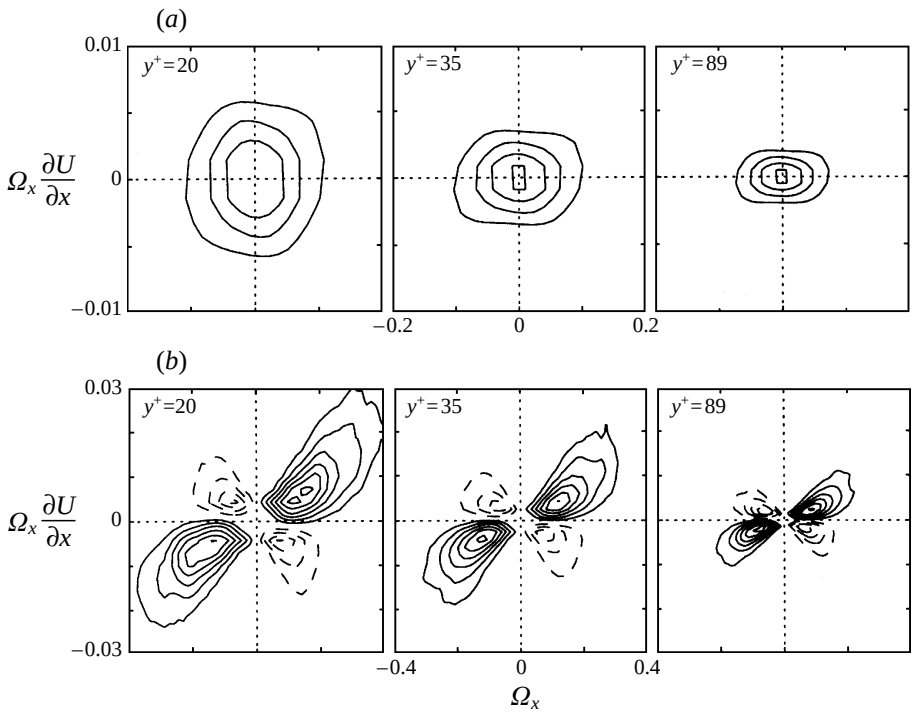

FIGURE 20. (*a*) JPDFs and (*b*) covariance integrands of Ω_x and $\Omega_x \partial U/\partial x$. Contour increments are (for $y^+ = 20$, 35 and 89, respectively) (*a*) 1.5×10^2, 2.4×10^2, 6.0×10^2 and (*b*) 2.4×10^{-7}, 1.9×10^{-7}, 6.7×10^{-8}. The outer contours are one increment above zero.

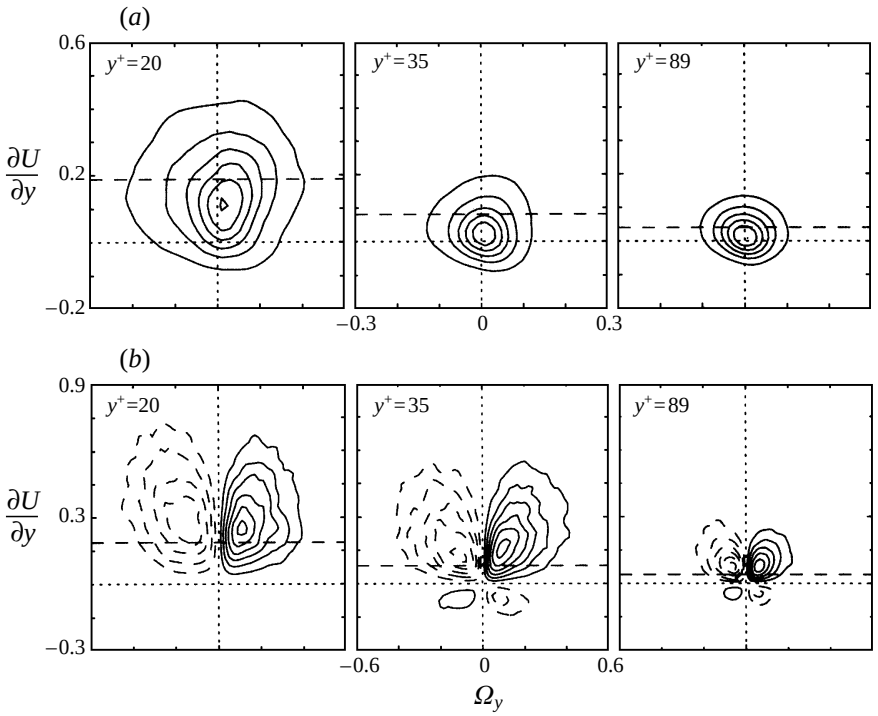

FIGURE 21. (*a*) JPDFs and (*b*) covariance integrands of Ω_y and $\partial U/\partial y$. Horizontal dashed lines (– – –) indicate $\partial\overline{U}/\partial y$ at each y^+ position. Contour increments (for $y^+ = 20$, 35 and 89, respectively) are (*a*) 1.8, 4.6, 8.6 and (*b*) 9.3×10^{-6}, 3.9×10^{-6}, 2.7×10^{-6}. The outer contours are one increment above zero.

in these values are due to measurement inaccuracies. The net $\overline{\Omega_x\Omega_x\partial U/\partial x}$ covariance values are thus all positive at $y^+ = 20, 35$ and 89. Indeed they are positive at all the measurement locations as was shown in figure 16(*a*). Therefore the $\partial U/\partial x$ strain acts to increase $(\pm\Omega_x)^2$ by stretching the vorticity filaments more than compressing them. In figures 20(*a*), 33(*a*) and 39(*a*), the JPDF contours should have a singularity at the origin for Ω_x, Ω_y and Ω_z identically zero, respectively. This does not appear in these figures because of the finite bin sizes. However, this deficiency in the plots has no effect on their interpretation.

Figure 21 shows that almost all the rate of change of $\pm\Omega_x$ by $\partial U/\partial y$ strain (see sketch in figure 17) is due to $+\partial U/\partial y$. There only are occasional occurrences of $-\partial U/\partial y$ of small magnitude; for these instances the fluid at levels further from the wall is instantaneously moving slower than that nearer the wall. Figure 17 demonstrates that, when Ω_x and Ω_y are of like sign, $+\partial U/\partial y$ strain stretches the vorticity filament, thereby increasing $\pm\Omega_x$. When Ω_x and Ω_y are of unlike sign, $+\partial U/\partial y$ compresses the vorticity filament so that $\pm\Omega_x$ decreases. That the rate of stretching is much greater than the rate of compression due to $\pm\partial U/\partial y$ strain is clearly seen in figure 22(*b*) where the covariance integrand $\Omega_x\Omega_y\partial U/\partial y P(\Omega_x, \Omega_y\partial U/\partial y)$ is plotted. With reference again to figure 17, it is evident that the large positive contributions to the covariance, $\overline{\Omega_x\Omega_y\partial U/\partial y}$, from Q1 and Q3 in figure 22 are increases of $(\pm\Omega_x)^2$ by stretching, and the smaller negative contributions from Q2 and Q4 are decreases of $(\pm\Omega_x)^2$ by compression. The net rate of change, $\partial(\frac{1}{2}\Omega_x)^2/\partial t$, due to this term is positive at all

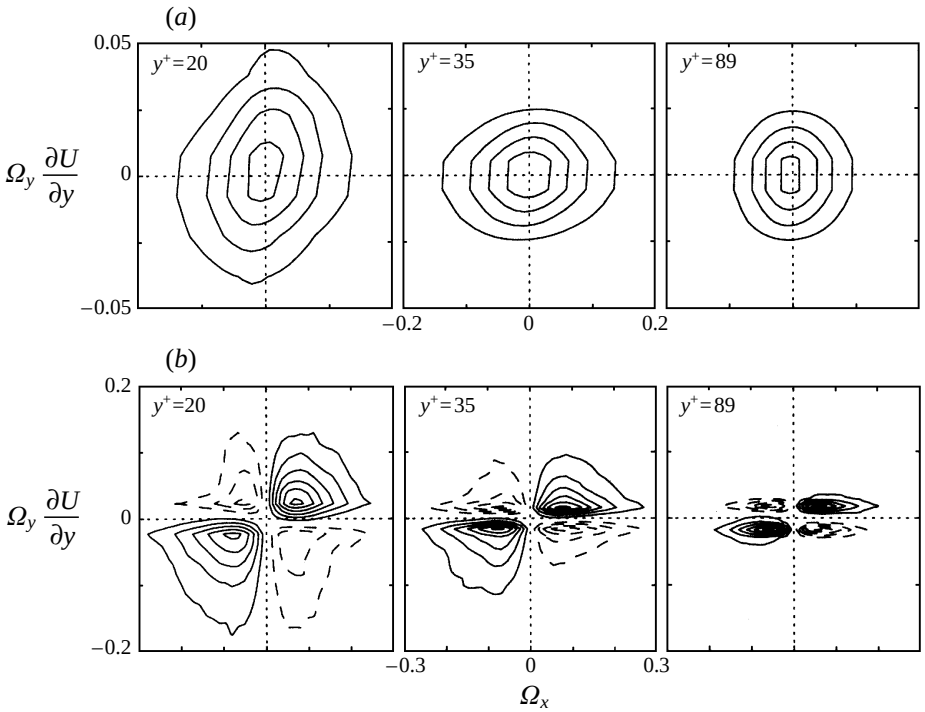

FIGURE 22. (*a*) JPDFs and (*b*) covariance integrands of Ω_x and $\Omega_y \partial U/\partial y$. Contour increments (for $y^+ = 20$, 35 and 89, respectively) are (*a*) 17, 28, 47 and (*b*) 1.3×10^{-6}, 7.2×10^{-7}, 4.8×10^{-7}. The outer contours are one increment above zero.

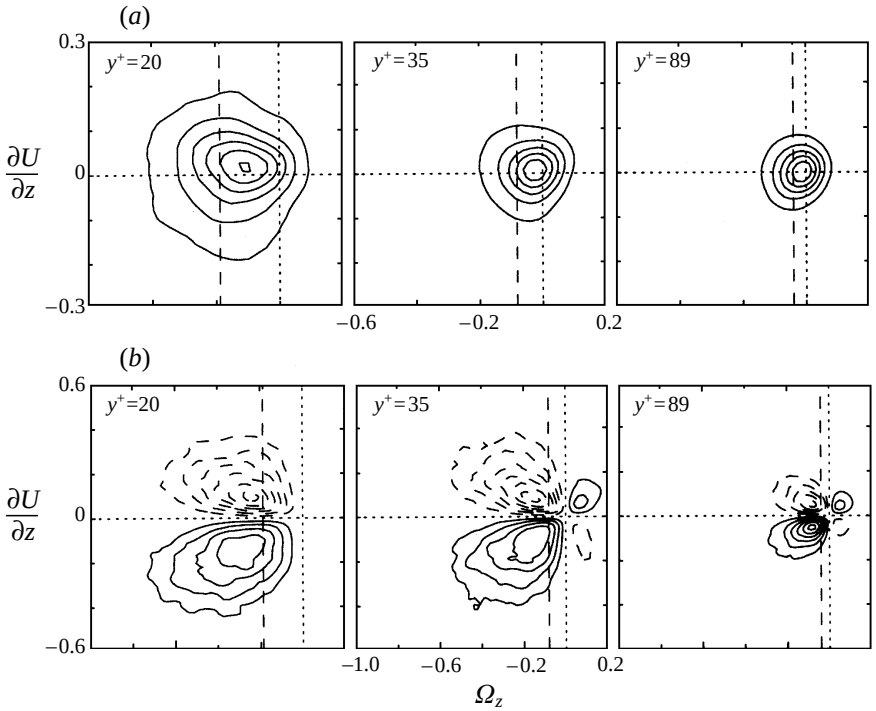

FIGURE 23. (*a*) JPDFs and (*b*) covariance integrands of Ω_z and $\partial U/\partial z$. Dashed lines (− − −) indicate $\overline{\Omega_z}$ at each y^+ position. Contour increments (for $y^+ = 20$, 35 and 89, respectively) are (*a*) 2.0, 4.9, 9.6 and (*b*) 9.2×10^{-6}, 4.2×10^{-6}, 2.9×10^{-6}. The outer contours are one increment above zero.

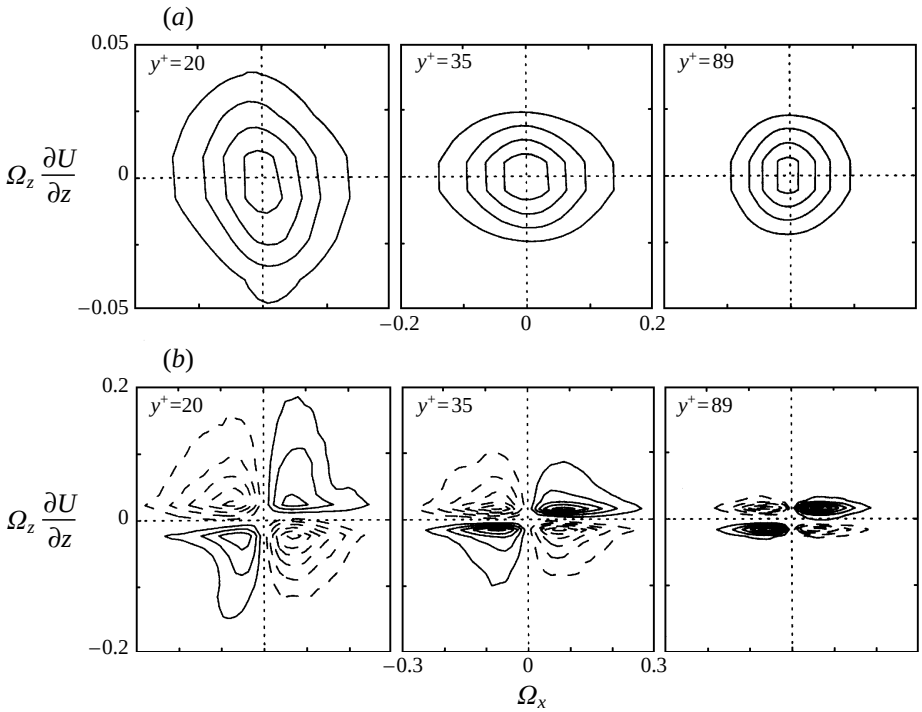

FIGURE 24. (*a*) JPDFs and (*b*) covariance integrands of Ω_x and $\Omega_z \partial U/\partial z$. Contour increments (for $y^+ = 20$, 35 and 89, respectively) are (*a*) 17, 28, 50 and (*b*) 1.2×10^{-6}, 6.5×10^{-7}, 4.1×10^{-7}. The outer contours are one increment above zero.

the measurement locations, as seen in figure 16(*a*), and quite large in the buffer layer. Indeed, this is the dominant stretching term.

The presence of the negative mean spanwise vorticity dominates the JPDFs in figure 23. Most of the Ω_z values are negative, but are distributed rather symmetrically about the horizontal ($\partial U/\partial z = 0$) axis as is required by the symmetry of the mean flow. With reference to the sketches in figure 18, it is apparent in figure 24(*b*) that the compression of $-\Omega_x$ by the straining action of $\pm\partial U/\partial z$ (Q2) and of $+\Omega_x$ by $\pm\partial U/\partial z$ (Q4) is greater than stretching (Q1 and Q3), especially nearer the wall. This is consistent with the distribution of the covariance $\overline{\Omega_x \Omega_z \partial U/\partial z}$ in figure 16(*a*), which is negative across the buffer layer, showing that compression dominates stretching of $\pm\Omega_x$ by $\pm\partial U/\partial z$ strain and that $(\pm\Omega_x)^2$ is decreased by this straining action.

Miyake & Tsujimoto (1996) have studied the relative strengths of the three terms $\Omega_x \partial U/\partial x$, $\Omega_y \partial U/\partial y$ and $\Omega_z \partial U/\partial z$ in equation (1.1) during the temporal evolution of a quasi-streamwise vortex detected in their DNS of a turbulent channel flow. In contrast to our results showing stretching of $\pm\Omega_x$ to be dominated by the term $\Omega_y \partial U/\partial y$, they find that by far their largest stretching term is $\Omega_x \partial U/\partial x$. However, our result is an average over our entire data sample, whereas theirs is a cross-stream area integral over the extent of the region in which $|\Omega_x|$ is greater than some chosen threshold. They do find, as do we, that the $\Omega_z \partial U/\partial z$ term results in a net compression of $\pm\Omega_x$.

Below $y^+ \approx 20$, Brooke & Hanratty (1993) found that, of the terms describing the time rate of change of fluctuating streamwise vorticity, the r.m.s. value of the term $\omega_y \partial u/\partial y$ is much greater than the r.m.s. values of $\omega_x \partial u/\partial x$ and $\omega_z \partial u/\partial z$. They used

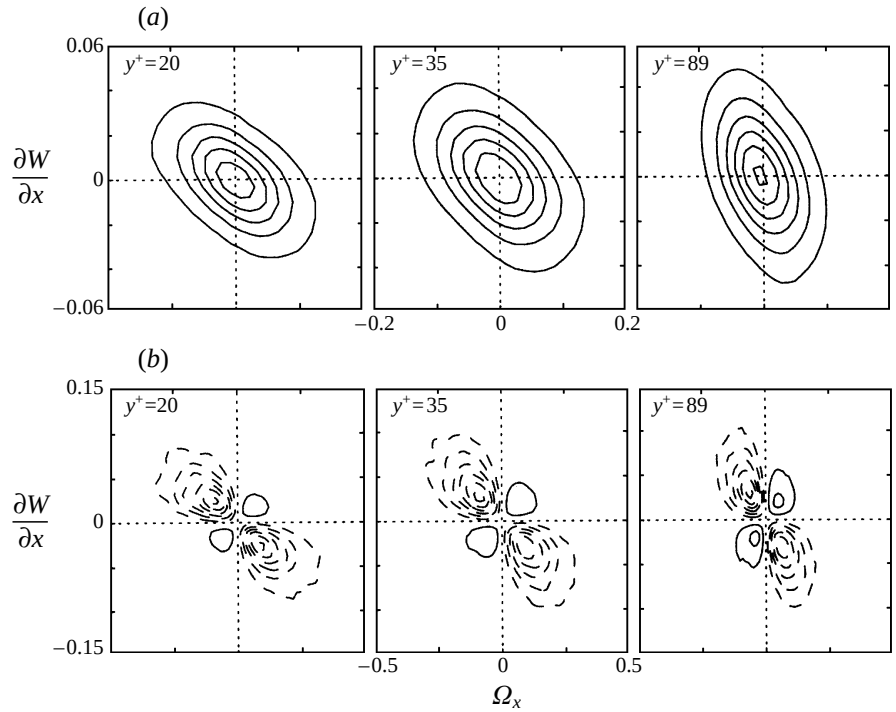

FIGURE 25. (*a*) JPDFs and (*b*) covariance integrands of Ω_x and $\partial W/\partial x$. Contour increments (for $y^+ = 20$, 35 and 89, respectively) are (*a*) 23, 18, 21 and (*b*) 1.2×10^{-6}, 1.2×10^{-6}, 8.1×10^{-7}. The outer contours are one increment above zero.

this fact as a criterion to detect newly created streamwise vortices in their turbulent channel flow DNS.

4.2.2. Ω_y^2 *rates of change by vorticity filament stretching/compression*

The summation of terms $\Omega_x \partial V/\partial x + \Omega_y \partial V/\partial y + \Omega_z \partial V/\partial z$ in the y-component of equation (1.1) expresses the rates of change of the Ω_y component of the vorticity vector due to stretching or compression by the velocity gradient field. Correspondingly, the rate of change of the Ω_y part of the enstrophy, $\partial(\frac{1}{2}\Omega_y^2)/\partial t$, is expressed by the sum of the terms $\Omega_y \Omega_x \partial V/\partial x + \Omega_y \Omega_y \partial V/\partial y + \Omega_y \Omega_z \partial V/\partial z$ in equations (1.2) and (4.3). As was seen in figure 16(*b*), the net rate of change of $\frac{1}{2}\Omega_y^2$ due to each of these terms is very nearly zero, and their sum is relatively small. This is due to a combination of smaller magnitudes of the covariances and, for the case of $\overline{\Omega_y \Omega_y \partial V/\partial y}$, approximate balance between vorticity filament stretching and compression. For completeness, these JPDFs and covariance integrand plots are included in Appendix B.

4.2.3. Ω_z^2 *rates of change by vorticity filament stretching/compression*

For the z-component of equation (1.1), the summation of terms $\Omega_x \partial W/\partial x + \Omega_y \partial W/\partial y + \Omega_z \partial W/\partial z$ expresses the rates of change of the Ω_z component of the vorticity vector due to reorientation by the $\partial W/\partial x$, $\partial W/\partial y$ and $\partial W/\partial z$ components of the velocity gradient field that stretch or compress the arbitrarily oriented vorticity filaments. Correspondingly, the sum of the terms $\Omega_z \Omega_x \partial W/\partial x + \Omega_z \Omega_y \partial W/\partial y + \Omega_z \Omega_z \partial W/\partial z$ in equations (1.2) and (4.3) expresses the rate of change of the Ω_z part of the enstrophy, $\partial(\frac{1}{2}\Omega_z^2)/\partial t$. In the first two terms of each of these

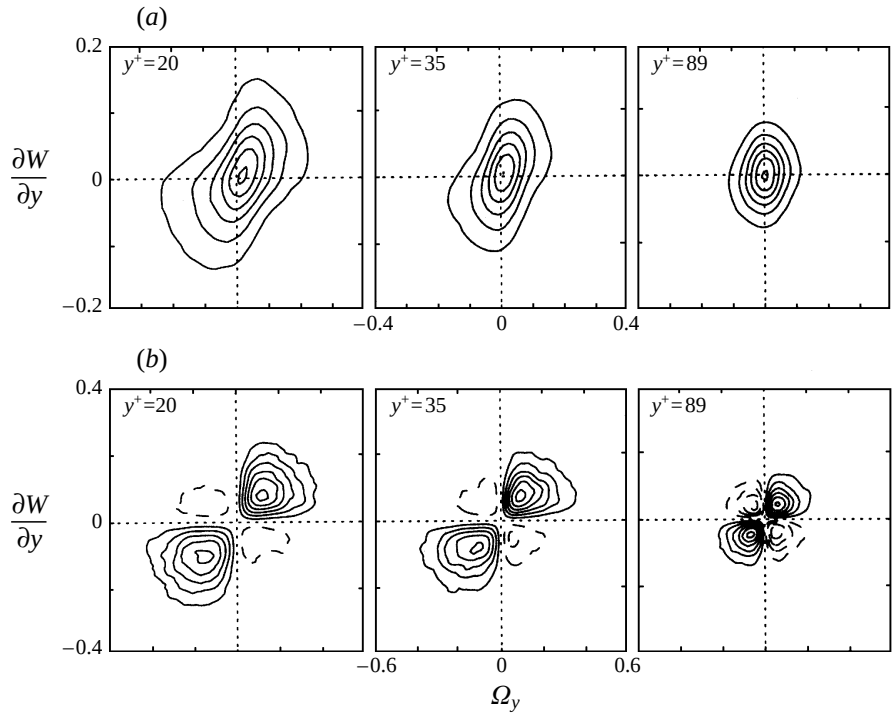

FIGURE 26. (*a*) JPDFs and (*b*) covariance integrands of Ω_y and $\partial W/\partial y$. Contour increments (for $y^+ = 20$, 35 and 89, respectively) are (*a*) 3.8, 5.9, 11 and (*b*) 2.4×10^{-6}, 2.1×10^{-6}, 9.5×10^{-7}. The outer contours are one increment above zero.

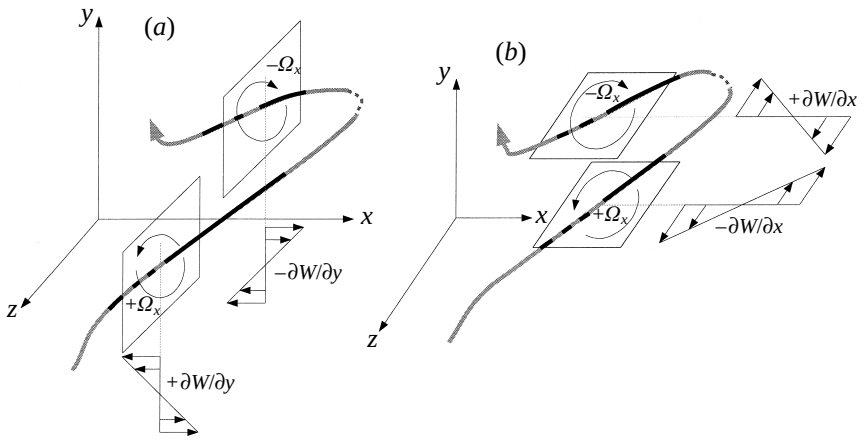

FIGURE 27. Illustration of a physical intepretation of the velocity gradient–vorticity correlations.

sums of three terms there are strong correlations between Ω_x and $\partial W/\partial x$ and between Ω_y and $\partial W/\partial y$. This is clearly seen in the orientations of the JPDFs: $P(\Omega_x, \partial W/\partial x)$ shown in figure 25(*a*), where Q2 and Q4 are the dominant quadrants, and $P(\Omega_y, \partial W/\partial y)$ in figure 26(*a*), where Q1 and Q3 are the dominant quadrants. These patterns of quadrant domination are also very clearly seen in covariance integrands, $\Omega_x \partial W/\partial x P(\Omega_x, \partial W/\partial x)$ and $\Omega_y \partial W/\partial y P(\Omega_y, \partial W/\partial y)$ respectively, shown

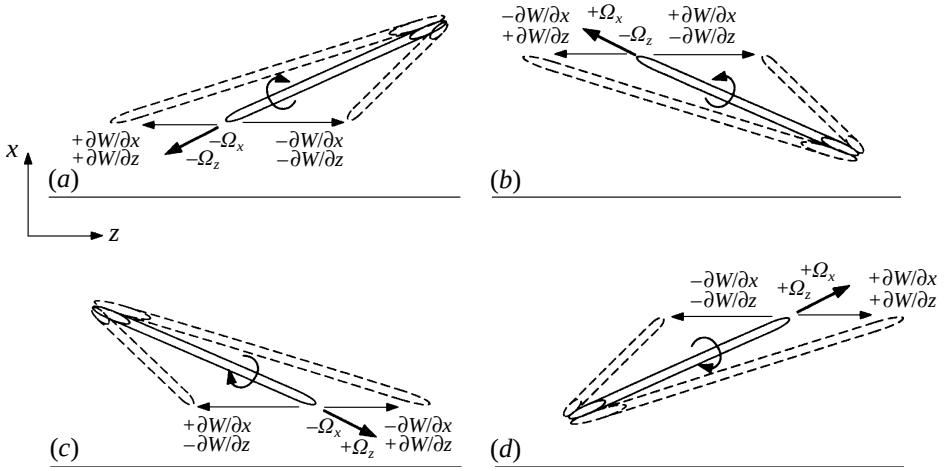

	Stretching	Figure 25	30	32	33	Compression	Figure 25	30	32	33
(*a*)	$-\Omega_z\ -\Omega_x\ +\frac{\partial W}{\partial x}$ or $+\frac{\partial W}{\partial z}$	Q2	Q3	Q2	Q3	$-\Omega_z\ -\Omega_x\ -\frac{\partial W}{\partial x}$ or $-\frac{\partial W}{\partial z}$	Q3	Q2	Q3	Q2
(*b*)	$-\Omega_z\ +\Omega_x\ -\frac{\partial W}{\partial x}$ or $+\frac{\partial W}{\partial z}$	Q4	Q3	Q2	Q3	$-\Omega_z\ +\Omega_x\ +\frac{\partial W}{\partial x}$ or $-\frac{\partial W}{\partial z}$	Q1	Q2	Q3	Q2
(*c*)	$+\Omega_z\ -\Omega_x\ -\frac{\partial W}{\partial x}$ or $+\frac{\partial W}{\partial z}$	Q3	Q1	Q1	Q1	$+\Omega_z\ -\Omega_x\ +\frac{\partial W}{\partial x}$ or $-\frac{\partial W}{\partial z}$	Q2	Q4	Q4	Q4
(*d*)	$+\Omega_z\ +\Omega_x\ +\frac{\partial W}{\partial x}$ or $+\frac{\partial W}{\partial z}$	Q1	Q1	Q1	Q1	$+\Omega_z\ +\Omega_x\ -\frac{\partial W}{\partial x}$ or $-\frac{\partial W}{\partial z}$	Q4	Q4	Q4	Q4

FIGURE 28. Set of possible orientations of projections of vorticity filaments on the (x, z)-plane being strained by $\pm\partial W/\partial x$ and $\pm\partial W/\partial z$ velocity gradients that change $\pm\Omega_z$.

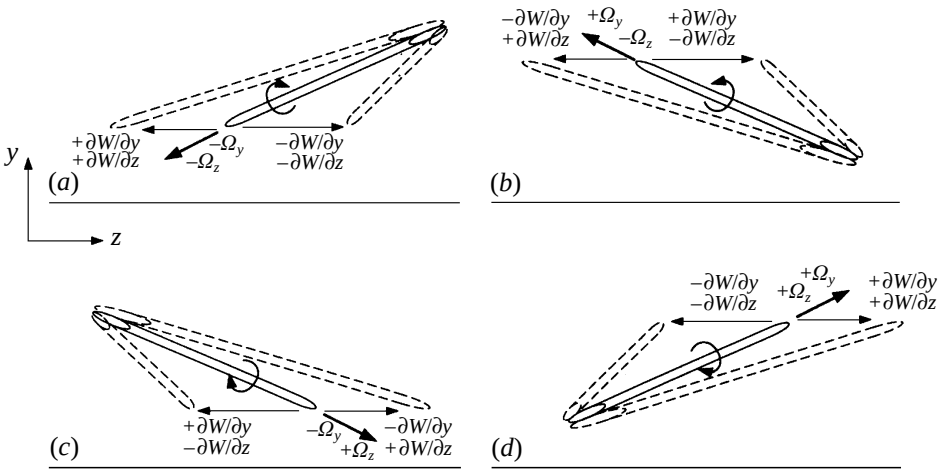

	Stretching	Figure 26	31	32	33	Compression	Figure 26	31	32	33
(*a*)	$-\Omega_z\ -\Omega_y\ +\frac{\partial W}{\partial y}$ or $+\frac{\partial W}{\partial z}$	Q2	Q3	Q2	Q3	$-\Omega_z\ -\Omega_y\ -\frac{\partial W}{\partial y}$ or $-\frac{\partial W}{\partial z}$	Q3	Q2	Q3	Q2
(*b*)	$-\Omega_z\ +\Omega_y\ -\frac{\partial W}{\partial y}$ or $+\frac{\partial W}{\partial z}$	Q4	Q3	Q2	Q3	$-\Omega_z\ +\Omega_y\ +\frac{\partial W}{\partial y}$ or $-\frac{\partial W}{\partial z}$	Q1	Q2	Q3	Q2
(*c*)	$+\Omega_z\ -\Omega_y\ -\frac{\partial W}{\partial y}$ or $+\frac{\partial W}{\partial z}$	Q3	Q1	Q1	Q1	$+\Omega_z\ -\Omega_y\ +\frac{\partial W}{\partial y}$ or $-\frac{\partial W}{\partial z}$	Q2	Q4	Q4	Q4
(*d*)	$+\Omega_z\ +\Omega_y\ +\frac{\partial W}{\partial y}$ or $+\frac{\partial W}{\partial z}$	Q1	Q1	Q1	Q1	$+\Omega_z\ +\Omega_y\ -\frac{\partial W}{\partial y}$ or $-\frac{\partial W}{\partial z}$	Q4	Q4	Q4	Q4

FIGURE 29. Set of possible orientations of projections of vorticity filaments on the (x, y)-plane being strained by $\pm\partial W/\partial y$ and $\pm\partial W/\partial z$ velocity gradients that change $\pm\Omega_z$.

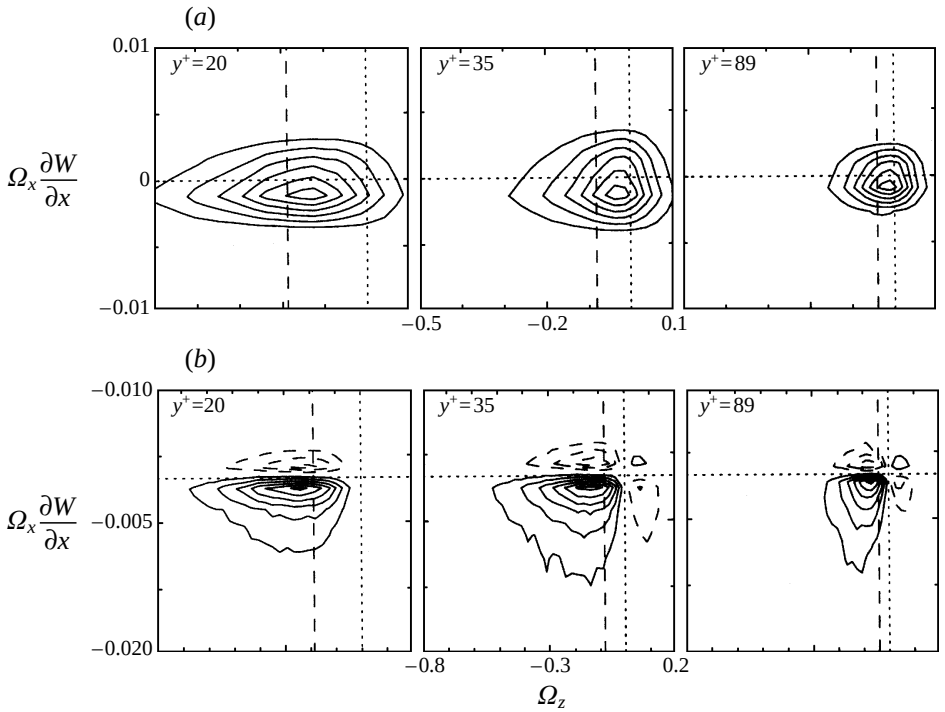

FIGURE 30. (*a*) JPDFs and (*b*) covariance integrands of Ω_z and $\Omega_x \partial W/\partial x$. Dashed lines (− − −) indicate $\overline{\Omega_z}$ at each y^+ position. Contour increments (for $y^+ = 20$, 35 and 89, respectively) are (*a*) 90, 121, 270 and (*b*) 1.4×10^{-6}, 8.0×10^{-7}, 4.0×10^{-7}. The outer contours are one increment above zero.

in figures 25(*b*) and 26(*b*). The strong correlation between Ω_x and $\partial W/\partial x$ is not surprising because $\partial W/\partial x$ is one of the gradients of Ω_y, which is itself rather strongly correlated with Ω_x (see figure 11). Figure 27(*b*) illustrates how the velocity field of vorticity filaments inclined downstream with strong Ω_x and Ω_y components results in this correlation. These inclined filaments have a velocity field with a strong $\partial W/\partial x$ velocity gradient that correlates with the Ω_x vorticity component of the vorticity filaments. Similarly, as illustrated in figure 27(*a*), because $\partial W/\partial y$ is one of the gradients of Ω_x, the velocity field of the same inclined vorticity filaments results in the strong positive correlation between Ω_y and $\partial W/\partial y$.

Figure 28, where the arbitrarily oriented vorticity filaments are projected on the (x, z)-plane, illustrates the stretching or compression of the filament by the straining action of the velocity gradients $\partial W/\partial x$ and $\partial W/\partial z$. Here $\pm\Omega_z$ is increased or decreased by the stretching or compression action of the strain. In figure 29 the projection of the arbitrarily oriented filament on the (y, z)-plane is sketched, and the stretching or compression by $\partial W/\partial y$ and $\partial W/\partial z$ is shown. These gradients also increase or decrease $\pm\Omega_z$.

That the stretching of $\pm\Omega_z$ by $\partial W/\partial x$ is much greater than compression by this gradient is made clear in figure 30, where the contributions to $\partial(\frac{1}{2}\Omega_z^2)/\partial t$ by this strain field are shown. Because the spanwise instantaneous vorticity, Ω_z, is predominantly negative, the covariance integrands, $\Omega_z \Omega_x \partial W/\partial x P(\Omega_z, \Omega_x \partial W/\partial x)$, show, with the help of reference to the sketches and table in figure 28, that Q3 stretching contributions to the covariance, $\overline{\Omega_z \Omega_x \partial W/\partial x}$ are by far the largest of the four quadrants. Thus the

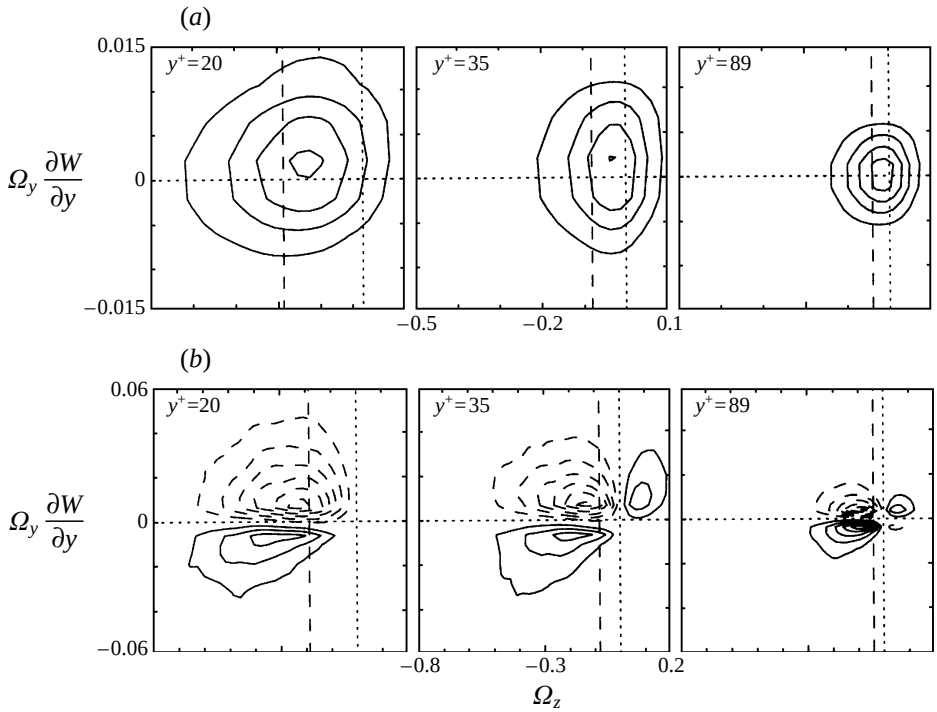

FIGURE 31. (*a*) JPDFs and (*b*) covariance integrands of Ω_z and $\Omega_y \partial W/\partial y$. Dashed lines (– – –) indicate $\overline{\Omega_z}$ at each y^+ position. Contour increments (for $y^+ = 20$, 35 and 89, respectively) are (*a*) 37, 64, 161 and (*b*) 1.5×10^{-6}, 8.6×10^{-7}, 3.0×10^{-7}. The outer contours are one increment above zero.

values of $\overline{\Omega_z \Omega_x \partial W/\partial x}$ are positive throughout the wall layer as shown in figure 16(*c*) and $\partial(\frac{1}{2}\Omega_z^2)/\partial t$ is a positive rate of enstropy increase due to this strain.

Near the wall, compression of $\pm\Omega_z$ by $\partial W/\partial y$ is much greater than stretching by this gradient as was shown in figure 16(*c*). The quadrant contributions to $\partial(\frac{1}{2}\Omega_z^2)/\partial t$ by this strain are given in figure 31. Here it is seen, with the help of reference to figure 29, that because the spanwise instantaneous vorticity, Ω_z, is predominantly negative, the covariance integrands, $\Omega_z \Omega_y \partial W/\partial y P(\Omega_z, \Omega_y \partial W/\partial y)$, show that Q2 compression and Q3 stretching contributions to the covariance, $\overline{\Omega_z \Omega_x \partial W/\partial x}$ are the largest of the four quadrants. The Q2 compression quadrant dominates at $y^+ = 20$, so the rate of change of enstrophy by this strain is negative.

The sketches in figure 29 and the JPDFs, $P(\Omega_z, \partial W/\partial z)$, and the covariance integrands, $\Omega_z \partial W/\partial z P(\Omega_z, \partial W/\partial z)$, in figure 32 illustrate that stretching of $\pm\Omega_z$ also results from the $+\partial W/\partial z$ gradient, while compression is caused by the $-\partial W/\partial z$ gradient. The contributions to $\partial(\frac{1}{2}\Omega_z^2)/\partial t$ by this strain are dominated by Q2 and Q3 in the covariance integrand, $\Omega_z \Omega_z \partial W/\partial z P(\Omega_z, \Omega_z \partial W/\partial z)$, of figure 33 because the instantaneous spanwise vorticity, Ω_z, is predominantly negative. As is apparent in figure 33 and in the distribution shown in figure 16(*c*), stretching (Q3) is significantly greater than compression (Q2) resulting in positive values of the covariance, $\overline{\Omega_z \Omega_z \partial W/\partial z}$, all across the wall layer and a positive rate of enstrophy increase by this straining process. Indeed, the stretching of $\pm\Omega_z$ by $+\partial W/\partial z$ is one of the largest contributors to the positive rate of change of the total enstrophy.

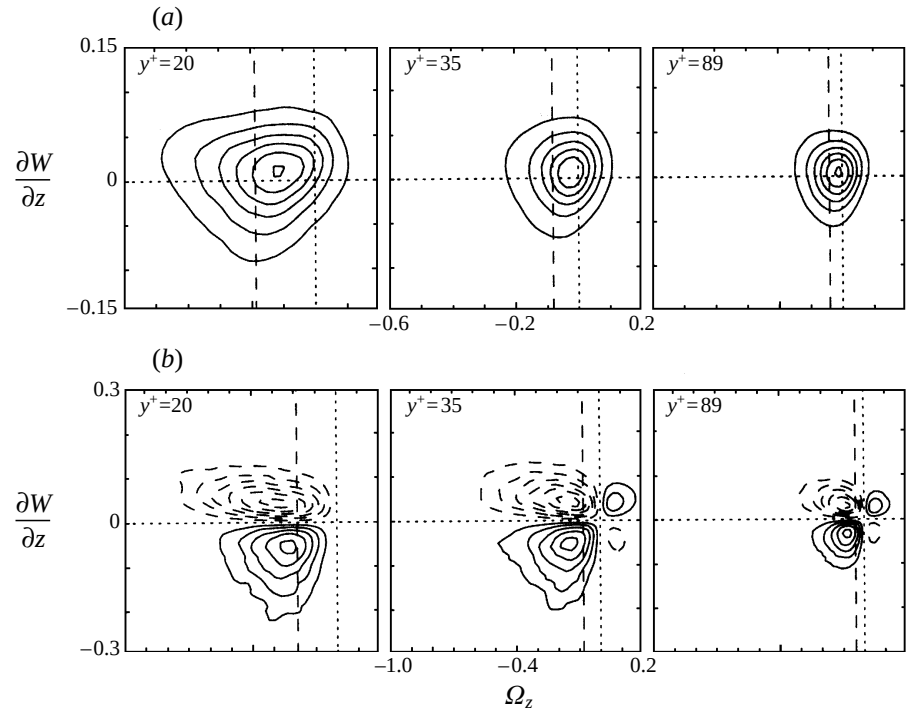

FIGURE 32. (*a*) JPDFs and (*b*) covariance integrands of Ω_z and $\partial W/\partial z$. Dashed lines (− − −) indicate $\overline{\Omega_z}$ at each y^+ position. Contour increments (for $y^+ = 20$, 35 and 89, respectively) are (*a*) 4.0, 8.0, 15 and (*b*) 5.1×10^{-6}, 2.5×10^{-6}, 1.3×10^{-6}. The outer contours are one increment above zero.

5. Conclusions

The present measurements of a number of statistical properties of the turbulent boundary layer velocity and vorticity fields compared quite favourably with published experimental and DNS results of other investigators. It was observed that the Reynolds number effects on the statistical properties, noted in the literature, are difficult to sort out because of the different methods by which the value of the friction velocity, used to scale the properties, is determined.

Joint probability density function and covariance integrand analysis was performed with various combinations of vorticity and vorticity–velocity gradient components. The results of this analysis indicated the following:

(*a*) A preferred orientation of the vorticity filaments in the wall layer of the turbulent boundary layer is evident. For example, the positive correlations shown in the JPDFs of the Ω_x and Ω_y vorticity components points to the preference for inclined, like-sign vorticity filaments. The filaments that contribute most to the covariance $\overline{\Omega_x\Omega_y}$ have angles of inclination to the x-coordinate axis that decrease with distance moving from the buffer to the logarithmic layer, while those that contribute most to the covariances $\overline{\Omega_x\Omega_z}$ and $\overline{\Omega_y\Omega_z}$, have angles of inclination to the z-coordinate axes that increase with distance from the wall. These patterns of vorticity filament orientation in the three coordinate planes are qualitatively consistent with observations of Bernard *et al.* (1993).

(*b*) The covariances $\overline{\Omega_i\Omega_j\partial U_i/\partial x_j}$ and the corresponding JPDFs, $P(\Omega_i, \Omega_j\partial U_i/\partial x_j)$, and covariance integrands, $\Omega_i\Omega_j\partial U_i/\partial x_j \cdot P(\Omega_i\Omega_j\partial U_i/\partial x_j)$ show that, on balance,

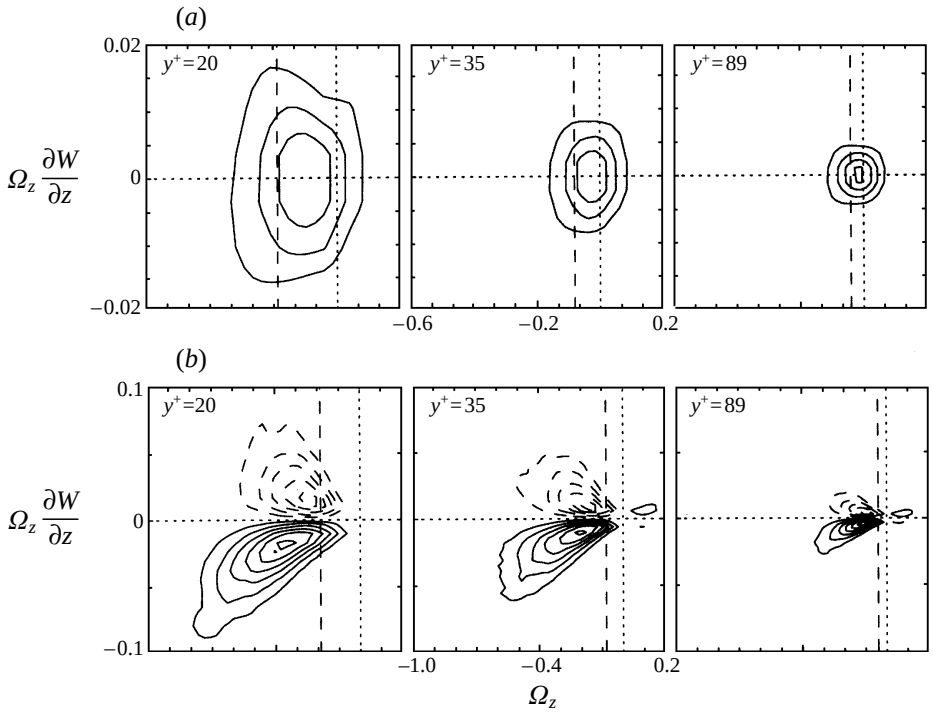

FIGURE 33. (*a*) JPDFs and (*b*) covariance integrands of Ω_z and $\Omega_z \partial W/\partial z$. Dashed lines (− − −) indicate $\overline{\Omega_z}$ at each y^+ position. Contour increments (for $y^+ = 20$, 35 and 89, respectively) are (*a*) 28, 85, 232 and (*b*) 3.0×10^{-6}, 9.4×10^{-7}, 3.4×10^{-7}. The outer contours are one increment above zero.

stretching dominates over compression of vorticity filaments yielding a positive rate of change of $(\pm\Omega_x)^2$ and $(\pm\Omega_z)^2$. The principal stretching-dominated covariances are $\overline{\Omega_x \Omega_y \partial U/\partial y}$ and $\overline{\Omega_z \Omega_z \partial W/\partial z}$, while the principal compression-dominated covariances are $\overline{\Omega_x \Omega_z \partial U/\partial z}$ and $\overline{\Omega_z \Omega_y \partial W/\partial y}$. The net rate of change of $(\pm\Omega_y)^2$ is small due to a combination of smaller magnitudes of the covariances and, for the case of the $\overline{\Omega_y \Omega_y \partial V/\partial y}$ covariance, approximate balance between vorticity filament stretching and compression.

This work has been supported by National Science Foundation Grant CTS-8911892. Professor Denis Jeandel made it possible for the experiments to be carried out at the Ecole Centrale de Lyon; Jean-Louis Balint was also very helpful in making these arrangements. Faouzi Laadhari greatly assisted us in performing the experiments. Several discussions with Peter Bernard led to the sketches shown in figure 27 to interpret these types of vorticity–velocity gradient correlations. Finally, Ron Panton, Javier Jimenez, Jim Brasseur and Brian Cantwell helpfully discussed with us interpretations of equation (4.3).

Appendix A. Data reduction method

The data reduction method of Marasli *et al.* (1993) begins with Jorgensen's (1971) expression for the effective cooling velocity for a hot-wire sensor inclined to the flow

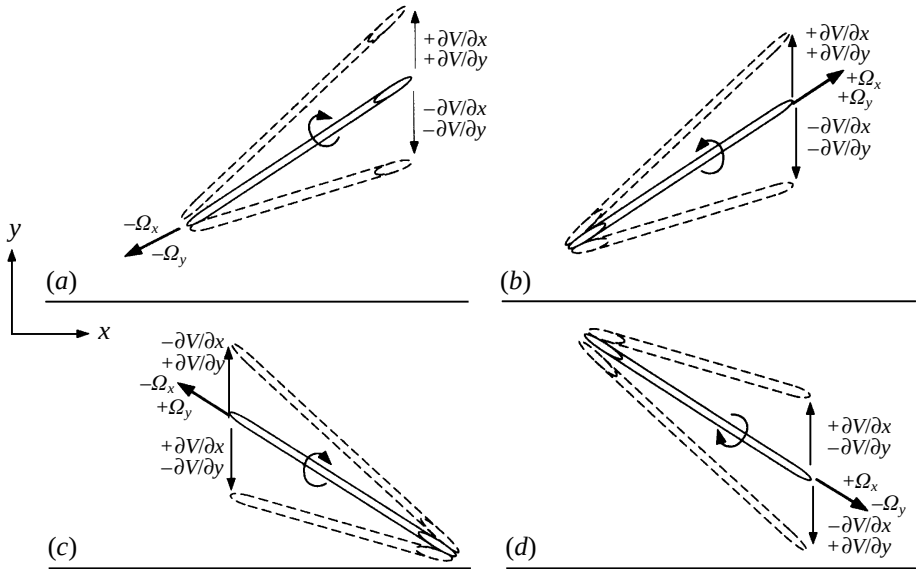

	Stretching	Figure 36	37	38	39	Compression	Figure 36	37	38	39
(*a*)	$-\Omega_y\ -\Omega_x\ +\frac{\partial V}{\partial x}$ or $+\frac{\partial V}{\partial y}$	Q2	Q3	Q2	Q3	$-\Omega_y\ -\Omega_x\ -\frac{\partial V}{\partial x}$ or $-\frac{\partial V}{\partial y}$	Q3	Q2	Q3	Q2
(*b*)	$+\Omega_y\ +\Omega_x\ +\frac{\partial V}{\partial x}$ or $+\frac{\partial V}{\partial y}$	Q1	Q1	Q1	Q1	$+\Omega_y\ +\Omega_x\ -\frac{\partial V}{\partial x}$ or $-\frac{\partial V}{\partial y}$	Q4	Q4	Q4	Q4
(*c*)	$+\Omega_y\ -\Omega_x\ -\frac{\partial V}{\partial x}$ or $+\frac{\partial V}{\partial y}$	Q3	Q1	Q1	Q1	$+\Omega_y\ -\Omega_x\ +\frac{\partial V}{\partial x}$ or $-\frac{\partial V}{\partial y}$	Q2	Q4	Q4	Q4
(*d*)	$-\Omega_y\ +\Omega_x\ -\frac{\partial V}{\partial x}$ or $+\frac{\partial V}{\partial y}$	Q4	Q3	Q2	Q3	$-\Omega_y\ +\Omega_x\ +\frac{\partial V}{\partial x}$ or $-\frac{\partial V}{\partial y}$	Q1	Q2	Q3	Q2

FIGURE 34. Set of possible orientations of projections of vorticity filaments on the (x, y)-plane being strained by $\pm\partial V/\partial x$ and $\pm\partial V/\partial y$ velocity gradients that change $\pm\Omega_y$.

direction

$$U_{eff}^2 = U_n^2 + k^2 U_t^2 + h^2 U_b^2, \tag{A 1}$$

where U_n, U_t and U_b are the normal, tangential and binormal (normal to the plane containing the prongs) components of the velocity vector with respect to the sensor. For a wire inclined to the flow coordinate axes,

$$U_n = n_1 U + n_2 V + n_3 W, \tag{A 2}$$

$$U_t = t_1 U + t_2 V + t_3 W, \tag{A 3}$$

$$U_b = b_1 U + b_2 V + b_3 W, \tag{A 4}$$

where, for an ideal probe, the coefficients n_l, t_l, b_l (l = 1–3) can be written in terms of sines and cosines of the angles of inclination of the wires to the flow coordinate axes. The sensitivity coefficients k and h, as defined by Jorgensen, must be obtained empirically. U, V and W are the velocity components in the mean flow, the wall normal and the spanwise directions, respectively. When equations (A 2)–(A 4) are substituted into equation (A 1), the coefficients n_l, t_l, b_l are coupled with k and h. The effective cooling velocity on the jth sensor (j = 1–9) then can be expressed as

$$U_{eff_j}^2 = a_{1j} U_j^2 + a_{2j} V_j^2 + a_{3j} W_j^2 + a_{4j} U_j V_j + a_{5j} U_j W_j + a_{6j} V_j W_j, \tag{A 5}$$

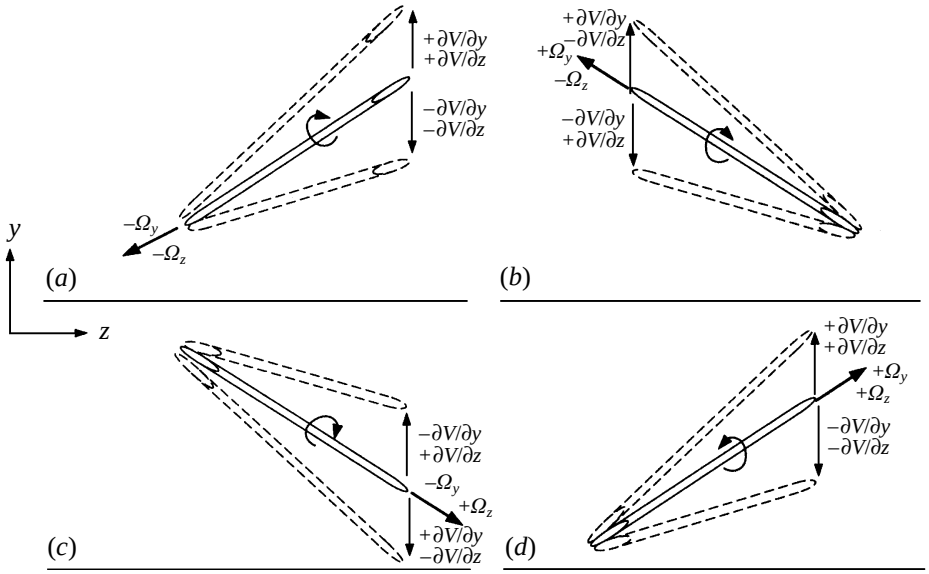

	Stretching	Figure 38	39	40	41	Compression	Figure 38	39	40	41
(*a*)	$-\Omega_y\ -\Omega_z\ +\frac{\partial V}{\partial y}$ or $+\frac{\partial V}{\partial z}$	Q2	Q3	Q2	Q3	$-\Omega_y\ -\Omega_z\ -\frac{\partial V}{\partial y}$ or $-\frac{\partial V}{\partial z}$	Q3	Q2	Q3	Q2
(*b*)	$+\Omega_y\ -\Omega_z\ +\frac{\partial V}{\partial y}$ or $-\frac{\partial V}{\partial z}$	Q1	Q1	Q3	Q1	$+\Omega_y\ -\Omega_z\ -\frac{\partial V}{\partial y}$ or $+\frac{\partial V}{\partial z}$	Q4	Q4	Q2	Q4
(*c*)	$-\Omega_y\ +\Omega_z\ +\frac{\partial V}{\partial y}$ or $-\frac{\partial V}{\partial z}$	Q2	Q3	Q4	Q3	$-\Omega_y\ +\Omega_z\ -\frac{\partial V}{\partial y}$ or $+\frac{\partial V}{\partial z}$	Q3	Q2	Q1	Q2
(*d*)	$+\Omega_y\ +\Omega_z\ +\frac{\partial V}{\partial y}$ or $+\frac{\partial V}{\partial z}$	Q1	Q1	Q1	Q1	$+\Omega_y\ +\Omega_z\ -\frac{\partial V}{\partial y}$ or $-\frac{\partial V}{\partial z}$	Q4	Q4	Q4	Q4

FIGURE 35. Set of possible orientations of projections of vorticity filaments on the (y, z)-plane being strained by $\pm\partial V/\partial z$ and $\pm\partial V/\partial y$ velocity gradients that change $\pm\Omega_y$.

where a_{ij} ($i = 1$–6) are coefficients which account for both geometric and thermal effects and which are determined by calibration, and the velocity components cooling each sensor, U_j, V_j and W_j, are assumed to occur at the midpoint of each sensor.

The effective cooling velocity for a hot-wire sensor is nonlinearly related to the bridge output voltage E_j. Following Marasli *et al.* (1993) this relationship is expressed here by a fourth-order polynomial

$$U^2_{eff_j} = P_j(E) = A_{1j} + A_{2j}E_j + A_{3j}E_j^2 + A_{4j}E_j^3 + A_{5j}E_j^4, \tag{A 6}$$

where A_{ij} are the polynomial coefficients of the jth sensor ($j = 1 - 9$). In this investigation the calibrations of the probe were limited to pure pitch or yaw in a uniform calibration flow field of specified speed. The VW term in equation (A 5), which requires mixed pitch and yaw values, was not obtained; therefore the coefficient a_{6j} was set equal to zero in this equation for the data reduction herein.

Because of the spatial variation of the velocity field, for a multi-sensor probe the instantaneous velocity components, U_j, V_j and W_j, experienced by each sensor are different. Assuming that the gradients are constant within the probe volume at a given instant, the velocity components occurring at the midpoint of each sensor can be estimated from a Taylor's series expansion to first order. This expansion about the probe centroid in the cross-stream plane, perpendicular to the probe axis and passing

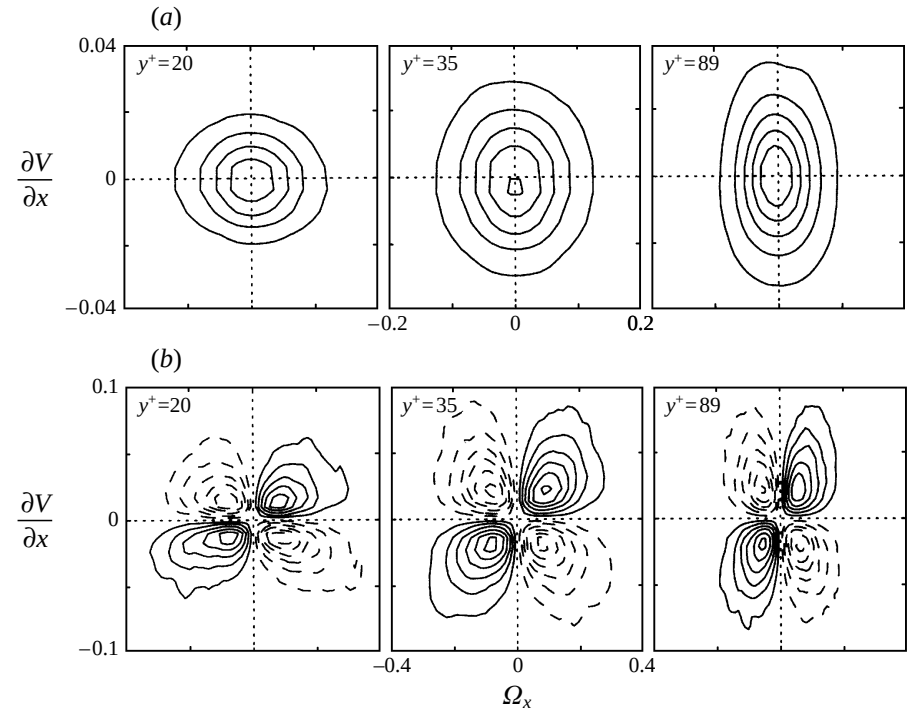

FIGURE 36. (*a*) JPDFs and (*b*) covariance integrands of Ω_x and $\partial V/\partial x$. Contour increments (for $y^+ = 20$, 35 and 89, respectively) are (*a*) 38, 24, 27 and (*b*) 5.4×10^{-7}, 7.9×10^{-7}, 4.5×10^{-7}. The outer contours are one increment above zero.

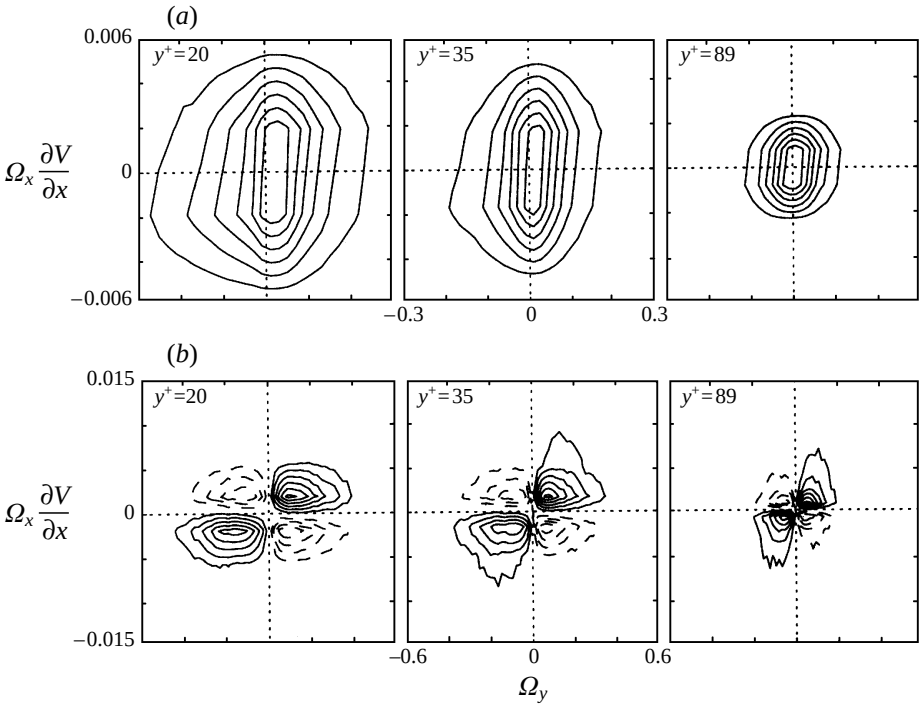

FIGURE 37. (*a*) JPDFs and (*b*) covariance integrands of Ω_y and $\Omega_x \partial V/\partial x$. Contour increments (for $y^+ = 20$, 35 and 89, respectively) are (*a*) 70, 108, 290 (*b*) 7.1×10^{-7}, 4.9×10^{-7}, 1.8×10^{-7}. The outer contours are one increment above zero.

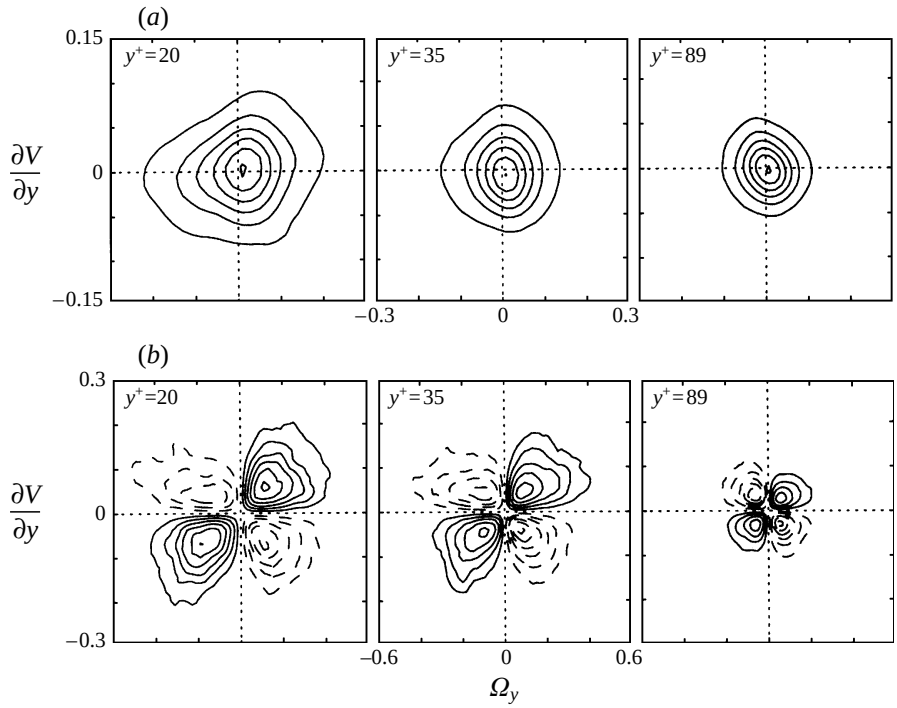

FIGURE 38. (*a*) JPDFs and (*b*) covariance integrands of Ω_y and $\partial V/\partial y$. Contour increments (for $y^+ = 20$, 35 and 89, respectively) are (*a*) 5.5, 8.8, 16 and (*b*) 1.7×10^{-6}, 1.4×10^{-6}, 8.6×10^{-7}. The outer contours are one increment above zero.

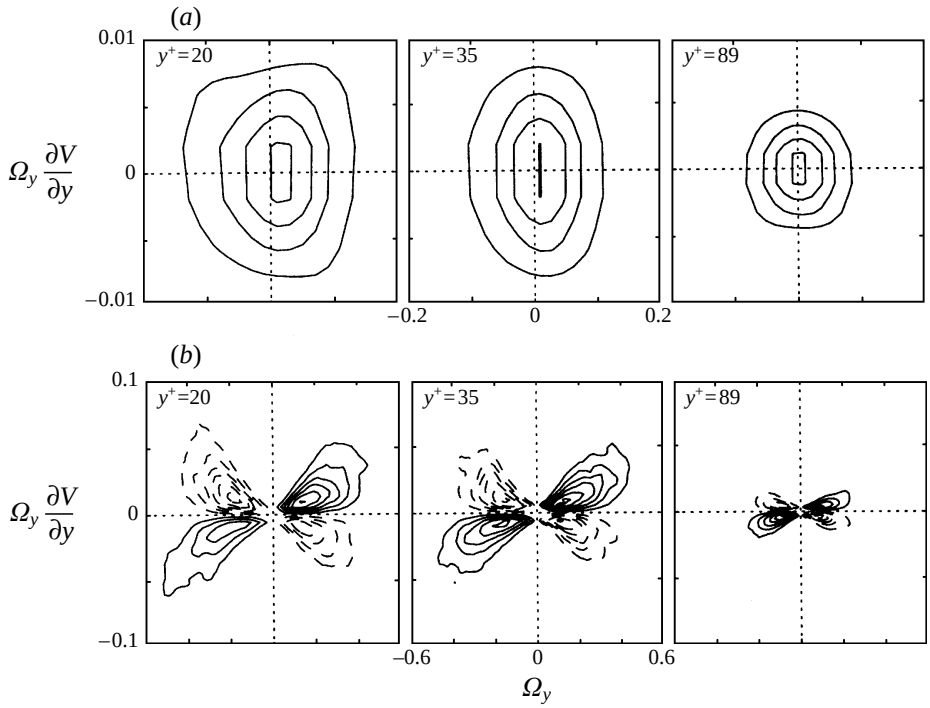

FIGURE 39. (*a*) JPDFs and (*b*) covariance integrands of Ω_y and $\Omega_y \partial V/\partial y$. Contour increments (for $y^+ = 20$, 35 and 89, respectively) are (*a*) 74, 103, 255 and (*b*) 5.4×10^{-7}, 3.2×10^{-7}, 1.6×10^{-7}. The outer contours are one increment above zero.

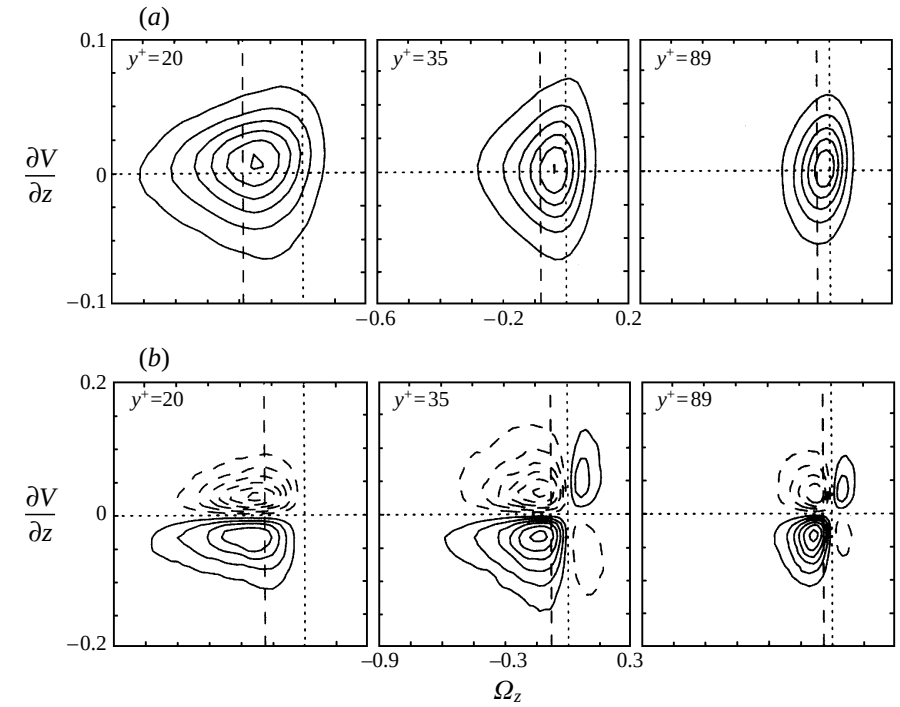

FIGURE 40. (*a*) JPDFs and (*b*) covariance integrands of Ω_z and $\partial V/\partial z$. Dashed lines (− − −) indicate $\overline{\Omega_z}$ at each y^+ position. Contour increments (for $y^+ = 20$, 35 and 89, respectively) are (*a*) 5.4, 7.8, 15 and (*b*) 4.6×10^{-6}, 2.2×10^{-6}, 1.5×10^{-6}. The outer contours are one increment above zero.

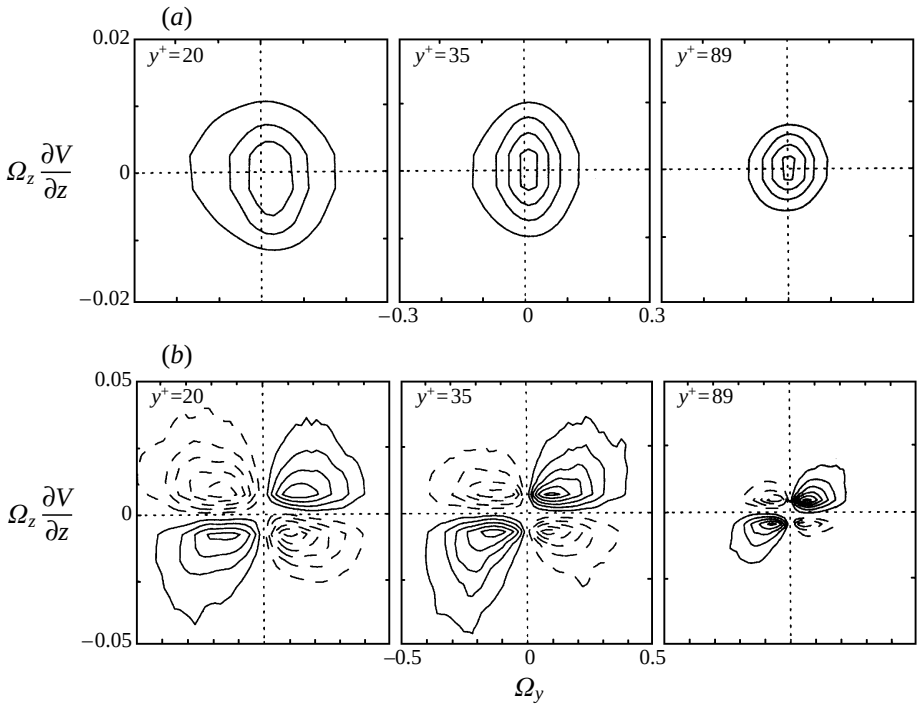

FIGURE 41. (*a*) JPDFs and (*b*) covariance integrands of Ω_y and $\Omega_z \partial V/\partial z$. Contour increments (for $y^+ = 20$, 35 and 89, respectively) are (*a*) 50, 74, 168 and (*b*) 5.4×10^{-7}, 3.2×10^{-7}, 2.0×10^{-7}. The outer contours are one increment above zero.

through the centre of each wire, gives

$$U_j = U_o + C_j \frac{\partial U}{\partial y} + D_j \frac{\partial U}{\partial z}, \tag{A 7}$$

$$V_j = V_o + C_j \frac{\partial V}{\partial y} + D_j \frac{\partial V}{\partial z}, \tag{A 8}$$

$$W_j = W_o + C_j \frac{\partial W}{\partial y} + D_j \frac{\partial W}{\partial z}, \tag{A 9}$$

where the coefficients C_j and D_j (j = 1–9) represent the spanwise and vertical displacements, which must be accurately measured, of the centres of each of the sensors from the probe centroid, and the velocity components U_o, V_o and W_o are those at the probe centroid. Substituting equations (A 7)–(A 9) into equation (A 5), equating this expression to the fourth-order polynomial of the voltages in equation (A 6) and rearranging yields 9 nonlinear algebraic equations with 9 unknowns: the three velocity components, U_o, V_o, W_o and the six velocity gradients in the cross-stream plane, $\partial U/\partial y$, $\partial U/\partial z$, $\partial V/\partial y$, $\partial V/\partial z$, $\partial W/\partial y$, and $\partial W/\partial z$. These nine equations (j = 1–9) can be expressed as

$$\begin{aligned} f_j = & -P_j + U_o^2 + 2C_j U_o \frac{\partial U}{\partial y} + 2D_j U_o \frac{\partial U}{\partial z} \\ & - a_{1j}\left[V_o^2 + 2C_j V_o \frac{\partial V}{\partial y} + 2D_j V_o \frac{\partial V}{\partial z}\right] \\ & - a_{2j}\left[W_o^2 + 2C_j W_o \frac{\partial W}{\partial y} + 2D_j W_o \frac{\partial W}{\partial z}\right] \\ & - a_{3j}\left[U_o V_o + 2C_j\left(U_o \frac{\partial V}{\partial y} + V_o \frac{\partial U}{\partial y}\right) + 2D_j\left(U_o \frac{\partial V}{\partial z} + V_o \frac{\partial U}{\partial z}\right)\right] \\ & - a_{4j}\left[U_o W_o + 2C_j\left(U_o \frac{\partial W}{\partial y} + W_o \frac{\partial U}{\partial y}\right) + 2D_j\left(U_o \frac{\partial W}{\partial z} + W_o \frac{\partial U}{\partial z}\right)\right] = 0. \end{aligned} \tag{A 10}$$

Piomelli, Balint & Wallace (1989) have demonstrated the acceptability of using Taylor's hypothesis to determine the streamwise gradients in wall-bounded flows in and above the buffer layer.

The coefficients A_{ij} (for the polynomial, P_j) and a_{ij} in equation (A 10) are obtained from calibration in a uniform steady flow of specified speeds in which the velocity gradients are negligibly small and the velocity components U_o, V_o and W_o are induced by pitching and yawing the probe. For this experiment the calibration was carried out in the nominally irrotational core flow of the wind tunnel. The calibration speed was varied at 0° pitch and yaw over a range from the highest (1.8 m s^{-1}) to the lowest (0.5 m s^{-1}) to be encountered in the boundary layer, and the pitch/yaw angles were varied through a range of $\pm 20°$ at fixed speeds of approximately 0.8, 1.0 and 1.2 m s^{-1}. Equations (A 10) were solved at each data sample time step by minimizing the error function given by $F = \sum f_j^2$ (j = 1–9). Newton's method was use to solve this system of nonlinear algebraic equations.

Appendix B. Ω_y^2 rates of change by vorticity filament stretching/compression

The stretching or compression of the vorticity filament by the straining action of the velocity gradients $\partial V/\partial x$ and $\partial V/\partial y$ is illustrated in figure 34 where the arbitrarily oriented filament is projected on the (x, y)-plane. Here, $\pm\Omega_y$ is increased or decreased by stretching or compression. The projection of the arbitrarily oriented filament on the (y, z)-plane is sketched in figure 35, where the stretching or compression by $\partial V/\partial y$ and $\partial V/\partial z$ is shown. This straining action also increases or decreases $\pm\Omega_y$.

The $P(\Omega_x, \partial V/\partial x)$ JPDFs in figure 36 are nearly symmetrically distributed about both axes ($\Omega_x = 0$ and $\partial V/\partial x = 0$). There is a clear dominance near the wall of stretching over compression of $\pm\Omega_y$ by $\partial V/\partial x$ as demonstrated by the larger contributions to the covariance $\overline{\Omega_y \Omega_x \partial V/\partial x}$ of Q1 and Q3 in figure 37. However, the magnitude of the peaks are very small, and the magnitude of the covariance is very close to zero all across the wall layer, as seen in figure 16(b). Thus $\pm\partial V/\partial x$ strain effects contribute very little to the net rate of change of Ω_y^2.

This dominance of stretching over compression is not as evident for $\pm\partial V/\partial y$ strain, as seen in figure 38 and figure 39, where the stretching and compression quadrants appear to contribute more nearly equally to the covariances $\overline{\Omega_y \partial V/\partial y}$ and $\overline{\Omega_y \Omega_y \partial V/\partial y}$, respectively. The fractional Q1 and Q3 (stretching) contributions in figure 39 at $y^+ = 35$ are $+2.18$ and $+1.94$ while those of Q2 and Q4 (compression) are -1.82 and -1.31. The $\overline{\Omega_y \Omega_y \partial V/\partial y}$ covariance values are nearly zero at all measurement locations, as shown in figure 16(b). The straining action of $\pm\partial V/\partial y$ (see figures 34 and 35) thus produces almost no net rate of change of $(\pm\Omega_y)^2$.

The prevalence of negative values of Ω_z again are seen in figure 40 where the $P(\Omega_z, \partial V/\partial z)$ JPDFs and $\Omega_z \partial V/\partial z \cdot P(\Omega_z, \partial V/\partial z)$ covariance integrands are plotted. They show some lack of symmetry about the horizontal ($\partial V/\partial z = 0$) axis due to measurement inaccuracies. Referring to the sketches and table in figure 35, the covariance integrand plots in figure 41 show a dominance of the stretching quadrants (Q1 and Q3) over the compression quadrants (Q2 and Q4), at $y^+ = 35$ and 89. However, the magnitude of the net covariance, $\overline{\Omega_y \Omega_z \partial V/\partial z}$, is very small for all measurement locations as seen in figure 16(b). Thus the straining action of the $\pm\partial V/\partial z$ velocity gradient on an arbitrarily oriented vorticity filament (see figure 35) produces almost no net rate of change of $(\pm\Omega_y)^2$.

REFERENCES

Balint, J.-L., Wallace, J. & Vukoslavčević, P. 1989 The statistical properties of the vorticity field of a two-stream mixing layer. In *Advances in Turbulence 2* (ed. H. H. Fernholz & H. E. Fiedler), pp. 74–78. Springer.

Balint, J.-L., Wallace, J. & Vukoslavčević, P. 1990 The transport of enstrophy in a turbulent boundary layer. In *Near-Wall Turbulence* (ed. S. J. Kline & N. Afgan), pp. 932–950, Dubrovnik. Zoran Zarić Memorial Conference, Hemisphere.

Balint, J.-L., Wallace, J. M. & Vukoslavčević, P. 1991 The velocity and vorticity vector fields of a turbulent boundary layer. Part 2. Statistical properties. *J. Fluid Mech.* **228**, 53–86.

Bernard, P. S., Thomas, J. M. & Handler, R. A. 1993 Vortex dynamics and the production of Reynolds stress. *J. Fluid Mech.* **253**, 385–419.

Blackwelder, R. & Haritonidis, J. 1983 Scaling of the bursting frequency in turbulent boundary layers. *J. Fluid Mech.* **132**, 87–103.

Brooke, J. W. & Hanratty, T. J. 1993 Origin of turbulence-producing eddies in a channel flow. *Phys. Fluids* A **5**, 1011–1022.

Coles, D. 1962 The turbulent boundary layer in compressible fluid. Appendix A: A manual of experimental practice for low speed flow. *Rand Rep.* R403R-PR, ARC24473.

Foss, J. & Wallace, J. 1989 The measurement of vorticity in transitional and fully developed turbulent flows. In *Lecture Notes in Engineering - Advances in Fluid Mechanics Measurements* (ed. M. Gad el Hak), vol. 45, pp. 263–321. Springer.

Gorski, J. J. & Bernard, P. S. 1996 Modeling of the turbulent enstrophy equation. *Intl J. Engng Sci.* **34**, 699–714.

Gorski, J. J., Wallace, J. M. & Bernard, P. S. 1994 The enstrophy equation budget of bounded turbulent shear flows. *Phys. Fluids* **6**, 3197–3199.

Handler, R. A., Hendricks, E. W. & Leighton, R. I. 1989 Low Reynolds number calculation of turbulent channel flow: a general discussion. *Naval Res. Lab. Mem. Rep.* 6410.

Jorgensen, F. 1971 Directional sensitivity of wire and fiber film probes. *DISA Information* **11**, 31–37.

Kastrinakis, E. G & Eckelmann, H. 1983 Measurements of streamwise vorticity fluctuations in a turbulent channel flow. *J. Fluid Mech.* **137**, 165–186.

Kim, J., Moin, P. & Moser, R. 1987 Turbulence statistics in fully developed channel flow at low Reynolds number. *J. Fluid Mech.* **177**, 133–166.

Klewicki, J. 1989 On the interactions between the inner and outer motions in turbulent boundary layers. PhD Dissertation, Michigan State University.

Kline, S. J., Reynolds, W. C., Schraub, F. A. & Runstadler, P. W. 1967 The structure of turbulent boundary layers. *J. Fluid Mech.* **30**, 741–773.

Marasli, B., Nguyen, P. & Wallace, J. 1993 A calibration technique for multiple-sensor hot-wire probes and its application to vorticity measurements in the wake of a circular cylinder. *Exps. Fluids* **15**, 209–218.

Miyake, Y. & Tsujimoto, K. 1996 Behavior of quasi-streamwise vortices in near-wall turbulence *ASME Fluids Engineering Div. Conf.* FED-Vol. 238, pp. 41–48.

Moin, P. & Kim, L. 1985 The structure of the vorticity field in turbulent channel flow. part 1: Analysis of instantaneous fields and statistical correlations. *J. Fluid Mech.* **155**, 441–464.

Piomelli, U., Balint, J.-L. & Wallace, J. 1989 On the validity of Taylor's hypothesis for wall-bounded turbulent flows. *Phys. Fluids* A **1**, 609–611.

Piomelli, U., Ong, L., Wallace, J. & Ladhari, F. 1993 Reynolds stress and vorticity in turbulent wall flows. *Appl. Sci. Res.* **51**, 365–370.

Purtell, L., Klebanoff, P. & Buckley, F. 1981 Turbulent boundary layer at low Reynolds numbers. *Phys. Fluids* **24**, 802–811.

Robinson, D. F., Harris, J. E. & Hassan, H. A. 1995 Unified turbulence closure model for axisymmetric and planar free shear flows. *AIAA J.* **33**, 2325–2331.

Spalart, P. 1988 Direct simulation of a turbulent boundary layer up to $Re_\theta = 1410$. *J. Fluid Mech.* **187**, 61–98.

Spalding, D. 1961 A single formula for the law of the wall. *Trans. ASME* C: *J. Appl. Mech.* **28**, 455–458.

Tennekes H. & Lumley, J. 1989 *A First Course in Turbulence.* MIT Press.

Vukoslavčević, P., Wallace, J. & Balint, J.-L. 1991 The velocity and vorticity vector fields of a turbulent boundary layer. Part 1. Simultaneous measurements by hot-wire anemometry. *J. Fluid Mech.* **228**, 25–51.

Walker, D. T., Leighton, R. & Garza-Rios, L. 1996 Shear-free turbulence near a flat free surface. *J. Fluid Mech.* **320**, 19-51.

Wallace, J. & Brodkey, R. 1977 Reynolds stress and joint probability density distributions in the u-v plane of a turbulent channel flow. *Phys. Fluids* **20**, 351–355.

Wallace, J., Eckelmann, H. & Brodkey, R. 1972 The wall region in turbulent shear flow. *J. Fluid Mech.* **54**, 39–48.

Wallace, J. & Foss, J. 1995 The measurement of vorticity in turbulent flows. *Ann. Rev. Fluid Mech.* **27**, 469–514.

Wei, T. & Willmarth, W. 1989 Reynolds number effects on the structure of a turbulent channel flow. *J. Fluid Mech.*, **204**, 57–95.

Willmarth, W. & Lu, S. 1972 Structure of the Reynolds stress near the wall. *J. Fluid Mech.* **55**, 65–92.